



# **NAVAL POSTGRADUATE SCHOOL**

**MONTEREY, CALIFORNIA**

## **THESIS**

### **FREE FIELD MODELING OF A MEMS-BASED PRESSURE GRADIENT MICROPHONE**

by

Stephen C.W. Harrison

December 2009

Thesis Advisor:  
Co-Advisor:

Gamani Karunasiri  
Steven R. Baker

**Approved for public release; distribution is unlimited**

<b>REPORT DOCUMENTATION PAGE</b>			<i>Form Approved OMB No. 0704-0188</i>	
Public reporting burden for this collection of information is estimated to average 1 hour per response, including the time for reviewing instruction, searching existing data sources, gathering and maintaining the data needed, and completing and reviewing the collection of information. Send comments regarding this burden estimate or any other aspect of this collection of information, including suggestions for reducing this burden, to Washington headquarters Services, Directorate for Information Operations and Reports, 1215 Jefferson Davis Highway, Suite 1204, Arlington, VA 22202-4302, and to the Office of Management and Budget, Paperwork Reduction Project (0704-0188) Washington DC 20503.				
<b>1. AGENCY USE ONLY (Leave blank)</b>		<b>2. REPORT DATE</b> December 2009	<b>3. REPORT TYPE AND DATES COVERED</b> Master's Thesis	
<b>4. TITLE AND SUBTITLE</b> Free Field Modeling of a MEMS-based Pressure Gradient Microphone			<b>5. FUNDING NUMBERS</b>	
<b>6. AUTHOR(S)</b> Stephen C.W. Harrison				
<b>7. PERFORMING ORGANIZATION NAME(S) AND ADDRESS(ES)</b> Naval Postgraduate School Monterey, CA 93943-5000			<b>8. PERFORMING ORGANIZATION REPORT NUMBER</b>	
<b>9. SPONSORING /MONITORING AGENCY NAME(S) AND ADDRESS(ES)</b> N/A			<b>10. SPONSORING/MONITORING AGENCY REPORT NUMBER</b>	
<b>11. SUPPLEMENTARY NOTES</b> The views expressed in this thesis are those of the author and do not reflect the official policy or position of the Department of Defense or the U.S. Government.				
<b>12a. DISTRIBUTION / AVAILABILITY STATEMENT</b> Approved for public release; distribution is unlimited			<b>12b. DISTRIBUTION CODE</b>	
<b>13. ABSTRACT</b> (maximum 200 words)  Several articles have been written on Micro Electro Mechanical System (MEMS) based microphones including directional sound sensors, mimicking the hearing of the fly, Ormia Ochracea. Determining the operating characteristics of such directional sound sensors requires an understanding of the interaction of the incident sound field with the MEMS structure. Previous work at the Naval Postgraduate School (NPS) concentrated on developing a finite element model that used either a force applied to the sound sensor or the far field of a point source to represent the acoustic pressure. However, both approaches failed to adequately explain experimental observations.  In this thesis, a compact model is developed using the COMSOL Multiphysics finite-element code to represent the incident plane sound wave, with a perfectly matched layer (PML) and radiation condition to eliminate sound energy reflection from the outer boundary.  The model was used to simulate the response of the sensor as a function of incident direction of the sound wave. The amplitude response of the sensor's bending frequency demonstrated a cosine dependence on the angle of incidence of the incoming sound wave. However, the amplitude at the sensor's rocking frequency showed a product of cosine and sine directional dependence. Finally, the substrate surrounding the sensor was introduced into the model. The introduction of the substrate resulted in increased amplitude response from the sensor. The simulated results including the substrate around the sensor agrees well with experimental measurements.  It was found experimentally that the sensor detects the sound pressure gradient (particle velocity), rather than pressure as originally envisioned.				
<b>14. SUBJECT TERMS</b> MEMS, Model, Simulation, Pressure Gradient, Particle Velocity, Directional, Microphone, COMSOL, Acoustic			<b>15. NUMBER OF PAGES</b> 69	
			<b>16. PRICE CODE</b>	
<b>17. SECURITY CLASSIFICATION OF REPORT</b> Unclassified	<b>18. SECURITY CLASSIFICATION OF THIS PAGE</b> Unclassified	<b>19. SECURITY CLASSIFICATION OF ABSTRACT</b> Unclassified	<b>20. LIMITATION OF ABSTRACT</b> UU	

THIS PAGE INTENTIONALLY LEFT BLANK

**Approved for public release; distribution is unlimited**

**FREE FIELD MODELING OF A MEMS-BASED PRESSURE GRADIENT  
MICROPHONE**

Stephen C.W. Harrison  
Lieutenant-Commander, Canadian Navy  
B. Eng, Royal Military College of Canada, 1992

Submitted in partial fulfillment of the  
requirements for the degrees of

**MASTER OF SCIENCE IN ENGINEERING ACOUSTICS  
and  
MASTER OF SCIENCE IN APPLIED PHYSICS**

from the

**NAVAL POSTGRADUATE SCHOOL  
December 2009**

Author: Stephen C.W. Harrison

Approved by: Gamani Karunasiri  
Thesis Advisor

Steven Baker  
Co-Advisor

Andres Larraza  
Chair, Department of Physics

Daphne Kapolka  
Chair, Engineering Acoustics Academic Committee

THIS PAGE INTENTIONALLY LEFT BLANK

## ABSTRACT

Several articles have been written on Micro Electro Mechanical System (MEMS) based microphones including directional sound sensors, mimicking the hearing of the fly, *Ormia Ochracea*. Determining the operating characteristics of such directional sound sensors requires an understanding of the interaction of the incident sound field with the MEMS structure. Previous work at the Naval Postgraduate School (NPS) concentrated on developing a finite element model that used either a force applied to the sound sensor or the far field of a point source to represent the acoustic pressure. However, both approaches failed to adequately explain experimental observations.

In this thesis, a compact model is developed using the COMSOL Multiphysics finite-element code to represent the incident plane sound wave, with a perfectly matched layer (PML) and radiation condition to eliminate sound energy reflection from the outer boundary.

The model was used to simulate the response of the sensor as a function of incident direction of the sound wave. The amplitude response of the sensor's bending frequency demonstrated a cosine dependence on the angle of incidence of the incoming sound wave. However, the amplitude at the sensor's rocking frequency showed a product of cosine and sine directional dependence. Finally, the substrate surrounding the sensor was introduced into the model. The introduction of the substrate resulted in increased amplitude response from the sensor. The simulated results including the substrate around the sensor agrees well with experimental measurements.

It was found experimentally that the sensor detects the sound pressure gradient (particle velocity), rather than pressure as originally envisioned.

THIS PAGE INTENTIONALLY LEFT BLANK

# TABLE OF CONTENTS

<b>I.</b>	<b>INTRODUCTION.....</b>	<b>1</b>
<b>A.</b>	<b>MOTIVATION .....</b>	<b>1</b>
<b>B.</b>	<b>THESIS ORGANIZATION.....</b>	<b>2</b>
<b>II.</b>	<b>BACKGROUND .....</b>	<b>3</b>
<b>A.</b>	<b>HEARING .....</b>	<b>3</b>
<b>B.</b>	<b>ORMIA OCHRACEA .....</b>	<b>4</b>
<b>C.</b>	<b>PREVIOUS WORK AT NPS.....</b>	<b>6</b>
<b>III.</b>	<b>THEORY .....</b>	<b>9</b>
<b>A.</b>	<b>BACKGROUND .....</b>	<b>9</b>
<b>B.</b>	<b>DYNAMIC PRESSURE MICROPHONE .....</b>	<b>11</b>
<b>C.</b>	<b>PRESSURE GRADIENT MICROPHONE.....</b>	<b>11</b>
<b>D.</b>	<b>PRESSURE GRADIENT MICROPHONE PHYSICS .....</b>	<b>12</b>
<b>IV.</b>	<b>MODELING AND SIMULATION.....</b>	<b>15</b>
<b>A.</b>	<b>OVERVIEW.....</b>	<b>15</b>
<b>1.</b>	<b>System Requirements .....</b>	<b>15</b>
<b>2.</b>	<b>COMSOL Software .....</b>	<b>16</b>
<b>a.</b>	<i>Overview .....</i>	<i>16</i>
<b>b.</b>	<i>Model Entry and Simulation Procedure .....</i>	<i>17</i>
<b>B.</b>	<b>NON-ACOUSTIC SIMULATIONS.....</b>	<b>17</b>
<b>1.</b>	<b>Model Construction .....</b>	<b>17</b>
<b>C.</b>	<b>ACOUSTIC/STRUCTURE COUPLED SIMULATIONS.....</b>	<b>25</b>
<b>1.</b>	<b>Model Construction .....</b>	<b>25</b>
<b>2.</b>	<b>Finite-element Model Optimization .....</b>	<b>29</b>
<b>a.</b>	<i>Spherical Volume 3D Model.....</i>	<i>30</i>
<b>b.</b>	<i>Hemispherical Volume .....</i>	<i>30</i>
<b>c.</b>	<i>Cylindrical Volume .....</i>	<i>31</i>
<b>d.</b>	<i>Meshing .....</i>	<i>31</i>
<b>e.</b>	<i>Change of Volume .....</i>	<i>34</i>
<b>f.</b>	<i>Perfectly Matched Layer.....</i>	<i>36</i>
<b>3.</b>	<b>Angle of Incidence.....</b>	<b>36</b>
<b>D.</b>	<b>INCLUSION OF SUBSTRATE.....</b>	<b>39</b>
<b>V.</b>	<b>EXPERIMENTAL DATA.....</b>	<b>45</b>
<b>A.</b>	<b>ANECHOIC CHAMBER.....</b>	<b>45</b>
<b>B.</b>	<b>RESONANT TUBE EXPERIMENT .....</b>	<b>45</b>
<b>VI.</b>	<b>CONCLUSIONS .....</b>	<b>49</b>
	<b>LIST OF REFERENCES.....</b>	<b>51</b>
	<b>INITIAL DISTRIBUTION LIST .....</b>	<b>53</b>



THIS PAGE INTENTIONALLY LEFT BLANK

## LIST OF FIGURES

Figure 1.	Location and external anatomy of the ears of <i>Ormia Ochracea</i> [From 1].	5
Figure 2.	General schematic of MEMS device [From 9].	6
Figure 3.	Omnidirectional polar pattern [From 15].	9
Figure 4.	Bi-directional polar pattern [From 15].	10
Figure 5.	Cardioid polar pattern [From 15].	10
Figure 6.	Acoustic wave incident on a small membrane with a finite baffle.	12
Figure 7.	2D view of the 4 <sup>th</sup> generation sensor used for simulation.	18
Figure 8.	3D model of the sensor in Figure 7.	18
Figure 9.	Incident pressure applied on top side of plates.	20
Figure 10.	Air damping pressure applied on bottom side of plates.	21
Figure 11.	Finite element mesh used for simulation.	21
Figure 12.	Rocking mode at 3,573 Hz.	22
Figure 13.	Bending mode at 4,013 Hz.	22
Figure 14.	Non-Acoustic broadband frequency response at 45-degree angle of incidence.	24
Figure 15.	Non-Acoustic rocking frequency response at 45-degree angle of incidence.	24
Figure 16.	Acoustic-Structure interaction application mode.	25
Figure 17.	3D acoustic volume with perfectly matched layer and the sensor at the center.	26
Figure 18.	Plot of incident plane wave in multiphysics at 200 kHz.	27
Figure 19.	Simulated amplitude at bending frequency.	29
Figure 20.	Measured amplitude at bending frequency [From 20].	29
Figure 21.	Hemispherical acoustic subdomain.	30
Figure 22.	Cylindrical acoustic subdomain.	31
Figure 23.	Subdomains used for meshing.	32
Figure 24.	Simulated amplitude and best-fit amplitude of the ipsilateral plate at the rocking frequency as a function of incident angle.	37
Figure 25.	Simulated amplitude as function of incident angle at bending frequency including substrate surrounding the sensor.	39
Figure 26.	Amplitude as a function of substrate width, length $7.5 \times 10^{-4}$ m.	41
Figure 27.	Amplitude as a function of substrate length, width $4 \times 10^{-3}$ m.	42
Figure 28.	Amplitude as a function of substrate area.	42
Figure 29.	Resonant tube experiment setup.	46

THIS PAGE INTENTIONALLY LEFT BLANK

## LIST OF TABLES

Table 1.	Parameters used for non-acoustic COMSOL simulations [From 11].	19
Table 2.	Silicon subdomain properties.	20
Table 3.	Non-Acoustic multiphysics simulation of amplitude of oscillations at rocking and bending frequencies for a 1 Pa incident plane sound wave.	23
Table 4.	Mesh configuration and best compromise for optimization of mesh.	33
Table 5.	Effects of reduction of thickness of cylinder used for acoustic domain.	34
Table 6.	Effects of change in cylinder radii.	35
Table 7.	Effects of removal of perfectly matched layer in simulations.	36
Table 8.	Amplitude as a function of incident angle at bending frequency with and without substrate around the sensor.	40

THIS PAGE INTENTIONALLY LEFT BLANK

## ACKNOWLEDGMENTS

I would like to thank Professor Gamani Karunasiri for his guidance and support throughout my time at the Naval Postgraduate School. He was a true mentor in helping me to understand not only the physics behind the research, but also the methodology to conduct proper research. He allowed me to conduct my research on my own, while overseeing my work and pointing me in the right direction when needed.

Also, I would like to thank Professor Steven Baker for his direction regarding the COMSOL Multiphysics acoustic module and for his assistance in the theoretical chapter of this thesis.

I would like to thank Professor Daphne Kapolka for her support in attaining a dual degree while at the Naval Postgraduate School. I would not have been able to achieve this goal without her assistance.

In addition, I would like to thank Professor Andres Larraza for his support in creating a schedule that would allow me to achieve a dual degree while at the Naval Postgraduate School.

Last, I would like to thank my wife, Shelley, and my children, Connor, Emily, and Carter, for their everlasting support and patience during my time at the Naval Postgraduate School.

THIS PAGE INTENTIONALLY LEFT BLANK

# I. INTRODUCTION

## A. MOTIVATION

What is the first thing that comes to your mind when you read the word *sound*? Is it a baby crying, people laughing, your favorite song, or perhaps someone calling your name? Sound is an amazing phenomenon of nature. But what is sound? It can be described as the passage of pressure fluctuations through a medium as the result of a driving oscillatory force.

The sound energy travels through the medium from the source to our ear. The ear funnels the sound energy onto our eardrum. The energy is passed from an air domain to a fluid domain and is then transmitted to our central nervous system. We can determine the approximate angle of arrival of the sound energy because we have two distinct ears. The sound energy will typically hit one ear first and then the other ear. Our brain calculates this angle subconsciously and we know from which angle the sound originated.

However, other types of animals or insects without the mammalian auditory system must use some other method of determining the direction that the sound came from. Throughout the millennia, natural selection provides a filter for determining which animals survive and which do not. If the animal's life depends on its hearing abilities, due to either mate selection or finding a source of food, then those animals with better hearing will prevail.

A small fly, *Ormia Ochracea*, has developed a unique sense of hearing, and continues to survive due to this ability, according to [1]. This fly has a very small auditory system that allows the fly to quickly and easily determine the angle of arrival of the incident sound. By mimicking this fly's hearing, we can produce a sound sensor with similar directional abilities.

A directional sound sensor that is on the millimeter scale could have numerous applications. Smaller hearing aids with better noise reduction are most likely the primary civilian user of such a sensor. There are numerous military applications for this device. The two most plausible applications could be an individual soldier sniper detection



system and an unmanned aerial vehicle reconnaissance system. Both of these applications need to have a small, sound sensor with a directional capability, and low mass and power requirements.

## **B. THESIS ORGANIZATION**

Chapter II of this thesis is devoted to a discussion of sound and hearing. The fly, *Ormia Ochracea*, and its anatomy, is discussed to demonstrate the reasons for researching a MEMS-based sound sensor. Further to this discussion, a thorough review of previous research conducted at the NPS that included design, development, modeling, simulation and experimentation is presented.

Chapter III provides details regarding the basic theory behind a transducer, polar patterns, a pressure microphone, and a pressure gradient microphone.

Chapter IV focuses on the modeling and simulation efforts. The computer hardware requirements are discussed followed by an overview of the finite element modeling software package, COMSOL Multiphysics [2]. The non-acoustic based model is reviewed for the purpose of providing some background information on past results. The acoustic model construction is covered along with the optimization techniques used to reduce the computation time required to achieve a simulation solution. Finally, the sensor is surrounded by a substrate to simulate a more realistic scenario.

Chapter V concentrates on the experimental data that has been collected from various sources. The experimental data provided by LCDR Michael Touse using the 5<sup>th</sup> generation of MEMS-based sensors at NPS is included for comparison purposes. A further brief experiment is discussed that provides a reasonable explanation of why this sensor is a particle velocity (pressure gradient) sensor as opposed to a pressure sensor.

The thesis concludes with a discussion regarding suggested future research into the simulation of MEMS-based sensors. Future work should concentrate on the damping of the sensor, working further with a sound source anywhere in a 3D environment and experimental work to investigate conclusively whether this sensor is a pressure gradient sensor or a combination of pressure and pressure gradient sensor.

## **II. BACKGROUND**

This thesis is primarily based upon a directional sensor that was designed at the Sensor Research Laboratory (SRL) of the NPS at Monterey, California. The program at NPS has resulted in several generations of MEMS-based devices being designed, manufactured and tested in a laboratory setting. This work has also resulted in the completion of several theses at NPS. This thesis expands on previous work done in the realm of simulation. The main goal of this thesis is twofold. First, it couples the incoming sound wave to the solid structure of the directional sensor. In the past, the sound wave was introduced into the simulation by two methods. Initial work introduced the sound wave as a force on the simulated sensor. Further work coupled the acoustic pressure to the device by using a point source, but due to spatial requirements between the sound source and sensor, simulation times were not practical. Second, this thesis attempts to optimize the processing times required for simulation. This will allow further modeling and simulation to gain a thorough understanding of the directional sensor.

### **A. HEARING**

Of course, we perceive sound using our sense of hearing. The human ear acts as the receiver for sound, and the middle portion of the ear amplifies the sound pressure. The translation of sound pressure from air to liquid occurs at the boundary between the middle ear and the inner ear, as the middle ear contains air and the inner ear is filled with fluid. The inner ear contains microscopic hairs that sense the pressure change and cause the release of chemical neurotransmitters when stimulated. In effect, the sound pressure waves are translated into nerve impulses that are decoded by the brain.

Other living creatures also use sound but for different purposes, including escaping predators, finding mates and locating prey. All of these actions rely on the ability of the creature to determine the direction that the sound came from. But how do they determine the direction of sound? In most mammals, including humans, the sound is localized within the central nervous system by comparing time of arrival differences and the loudness from each ear. If one estimates the human head width to be approximately

17 cm from ear to ear, then one can calculate the time of arrival difference along the midline of the head to be approximately 500 microseconds given the velocity of sound in air to be 343 m/s. Now, let us examine the wavelength of a 3,000 Hz sound signal, which is approximately 11 cm. Since this wavelength is less than the width of a human head, then there will also be pressure difference due to diffraction and scattering about the head. As well, there will be more than one wavelength between our ears and one should be able to easily detect the pressure amplitude difference as well as arrival time difference between the left and right ears.

## **B. ORMIA OCHRACEA**

*Ormia Ochracea* is a parasitic fly common to the southern United States and Mexico. Most recently it has been found on the island of Kauai in Hawaii, where it has devastated the population of chirping crickets [3]. This small, yellow fly has an incredible ability to determine the direction of sound. This ability is absolutely crucial to the fly's existence, as it is a parasitic fly that lays its larvae on a live, male cricket [4]. In order to reproduce, the female fly must do the same as a female cricket, namely, locate a male cricket. It finds the male cricket usually at dusk or dawn while the male cricket is chirping to attract female crickets. The fly hones in on the chirping cricket, lands close to the cricket and then walks the remaining few inches to mount the cricket and deposit the larvae [5].

Since 1992, R.N. Miles has written several journal articles describing *Ormia Ochracea* and its unique directional sound sensing ability. Specifically, Miles et al. [1] described the anatomy and physiology of the fly.

The fly's body is less than 1 cm in length and the hearing organ is approximately 1.5 mm across. The time difference of arrival for 5 kHz sound is approximately 4 microseconds, and the amplitude difference in the sound wave over a 1.5 mm distance is extremely difficult if not impossible to distinguish [6]. If the fly did, in fact, have the mammalian anatomy for directionally-selective hearing, then it would not be possible to determine the direction of sound. So how does the fly determine the direction of sound?

First, we need to examine the fly's auditory anatomy. It consists of a complex array of physiological mechanisms that convert acoustic energy in the sound field into mechanical vibrations that are sensed by the auditory sensory organs. As shown in Figure 1, the fly's hearing organ is located in front and between the first segment of the leg of the fly (coxae), below the neck and behind the head.

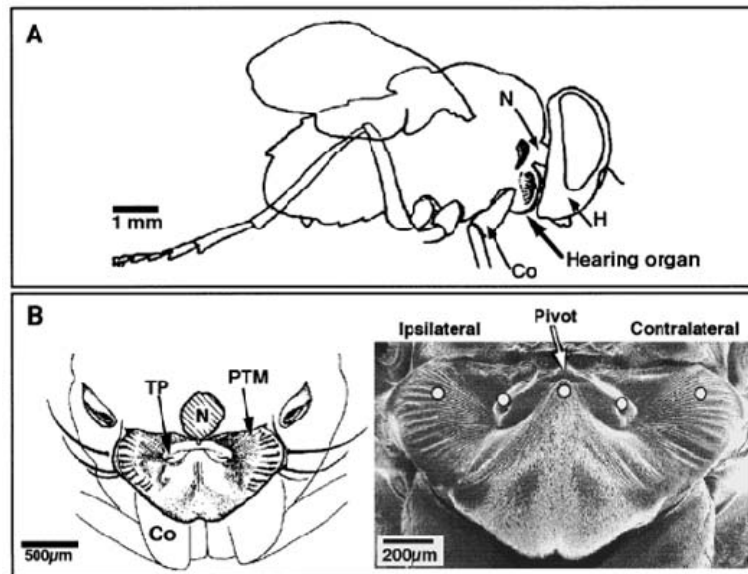


Figure 1. Location and external anatomy of the ears of *Ormia Ochracea* [From 1].

The fly has two prosternal tympanic membranes (PTMs or eardrums) that are the main receivers for sound energy. These membranes are connected to a pair of auditory sensory organs, the bulbae acusticae, which are located within a common, air-filled chamber. The bulbae acusticae attach to the membranes via a ridge-like ingrowth of the exoskeleton (apodeme), which resembles a stiff rod. In effect, the PTM receives the signal and transfers the sound energy through the rod activating the bulbae acusticae. Each bulba acustica contains 70–75 auditory receptor cells, which transfer the signals to the nervous system of the fly [1]. A detailed description of the anatomy is described by Robert et al [7].

The key to the fly's auditory system is the mechanical connection between the two PTMs known as the intertympanic bridge. As the incident sound wave hits the PTM closest to the sound source (ipsilateral), the PTM furthest from the sound source

(contralateral) is forced to move in the opposite direction via the intertympanal bridge. This motion would resemble a playground seesaw. As the sound wave comes in contact with the contralateral PTM, which has already been displaced due to the mechanical connection between the PTMs, it is forced in the opposite direction. This causes a bending motion about the intertympanal bridge. In effect, the PTM closest to the sound will achieve greater amplitude than the PTM furthest from the sound. As a result, the neural sensory cells in the ear closest to the sound will fire with dramatically less latency than those of the opposite ear [8].

### C. PREVIOUS WORK AT NPS

The SRL group has been developing MEMS devices over the last few years and is currently on the 5<sup>th</sup> generation of sound sensor. Figure 2 shows a general schematic of a 1<sup>st</sup> generation sensor with perforated sensor plates.

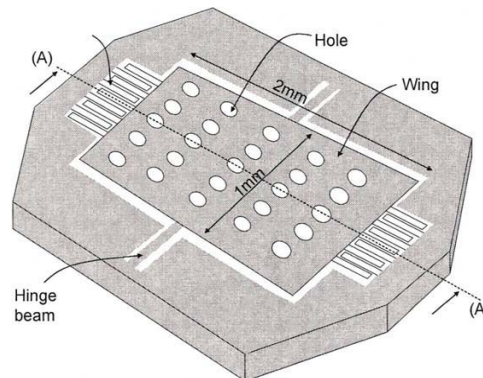


Figure 2. General schematic of MEMS device [From 9].

There have been five theses at NPS regarding MEMS directional sound sensors. Four of the theses were mentored by Professor Gamani Karunasiri and one by Professor Daphne Kapolka. Two of these theses included design, simulation, fabrication and testing of a biomimetic MEMS device based on *Ormia Ochracea*. Other theses involved experimentation, simulation and networking of various devices. There is also one PhD candidate working with the current generation of sensor.

LT Timothy Shivok's (United States Navy) thesis involved the design, fabrication and testing of "MEMS PolyMUMPs-based Miniature Microphone for Directional Sound

Sensing” [10]. Shivok started with 2 mm by 1 mm sensor wings which included several holes to eliminate squeeze film damping. Shivok incorporated additional designs with various geometric changes to the number and size of holes as well as the length and width of the cantilever beams. He used the COMSOL Multiphysics finite element modeling (FEM) code as the tool for simulation. Shivok’s experimentation showed lower amplitudes than simulation results. As a part of the simulation, the sound wave was represented by applying an equivalent force to the sensor surface. At the time, he concluded that the amplitude difference between simulation and experiment was in fact due to the methodology of introducing the sound wave into the simulation. However, further experimentation showed that the displacement amplitude was low due to weak sound coupling, due to relatively large holes on the wings.

As a follow-on to Shivok’s work, LT Antonios Dristas’ (Hellenic Navy) thesis was entitled “Characterization of the MEMS Directional Sound Sensor Fabricated Using the SOIMUMPS Process” [11]. Fifteen different designs were included on a single chip for experimentation purposes. Solid plate designs were included to compare with perforated plate designs. The sensors were fabricated using the SOIMUMPs fabrication process where the substrate under the sensors with solid wings was removed to reduce squeeze film damping. Once again, the sound wave was simulated by applying a force to the sensor surface. The simulated results for the rocking mode were in good agreement with the experimental results obtained. However, the perforated plate design again resulted in decreased amplitude response. It was also found that the edges of the wings touch the substrate underneath due to curling as a result of residual thermal stress during the processing. Finally, Dristas demonstrated experimentally that the incident angle could be determined by comparing the relative rocking and bending mode amplitudes. However, due to their narrow band response, the two modes had to be excited with a chirp signal from 2 to 14 kHz.

LT Dimitrios Chatzopoulos’ (Hellenic Navy) thesis entitled “Modeling the Performance of MEMS Based Directional Microphones” [12] furthered the simulation work of the previous students. He attempted to couple the acoustic and solid domains within COMSOL to more accurately model the sound field and solid sensor interaction.

This was a new and novel approach to the problem of the introduction of the sound wave into the simulation. However, he was hampered by acoustic reflections from the outer boundaries in his simulation. Further simulations using a point source and spherical acoustic domain rather than a radiating source in a rectangular domain provided better results. He was also the first to propose the acoustic particle velocity as the primary forcing function of these vibrations. However, simulation times were on the order of days which resulted in a limited number of simulations. In addition, he ran simulations whereby he altered the damping coefficients, introduced perforated plates, and created a resonant cavity to increase the amplitude response.

LT Norbahrin Muamad's (Brunei Navy) thesis entitled "Characterization of a MEMS Directional Microphone with Solid and Perforated Wings" [13]. Muamad used a 4th generation sensor chip that contained 12 different designs for experimentation. The sensors were fabricated again using the SOIMUMPs fabrication process where the substrate under all the sensors was removed. He focused on two devices; one with perforated wings and one with solid wings. He used an angle of incidence of 45 degrees to experimentally measure the amplitude response of the rocking and bending frequencies for both devices. Both sensors showed good response, indicating the small holes on the wings do not reduce the sound coupling. LT Kursad Simsek's (Turkish Army) thesis was entitled "Developing a Capacitance Readout Circuitry for a Directional MEMS Sound Sensor and Sound Source Localization in a Sensor Network Environment" [14]. The two main goals of this thesis, as the title suggests, were to introduce a readout for the sensor and to introduce the sensor into a network configuration. I will not expand more on this thesis as it does not pertain as closely to this thesis.

Lieutenant Commander Michael Touse (United States Navy) is currently working with the 5th generation sound sensor and has not yet completed his PhD dissertation.

### III. THEORY

#### A. BACKGROUND

A transducer converts one form of energy into another form of energy for various purposes. A microphone converts sound (acoustical pressure waves) into electrical signals that are proportional to the incident sound pressure. All microphones have a membrane or other element that vibrates due to the acoustic wave fronts that are incident upon it. A sensor in the microphone measures the vibrating element and converts the mechanical motion into electrical signals. What is done with the electrical signals is dependent on the application. One could amplify the signal for a rock concert, transmit the signal for a telephone conversation or further process the signal as in the Rock Band video game to determine how well the song was sung.

There are different kinds of microphones with various directivity or polar patterns. The polar pattern indicates how sensitive the microphone is to sound arriving at different angles from its axis. Various patterns include omnidirectional, bi-directional, cardioid, hyper-cardioid, sub-cardioid, super-cardioid, and shotgun to name a few. They all have strengths and weaknesses dependent upon the application they would be used for. Figures 3 to 5 show a few of these polar patterns with brief descriptions.

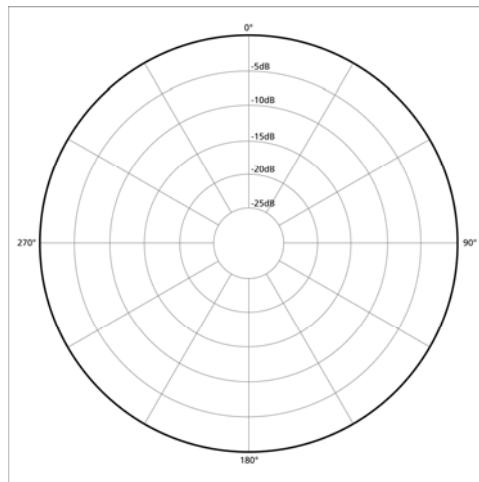


Figure 3. Omnidirectional polar pattern [From 15]



In theory, the omnidirectional polar pattern, as shown in Figure 3, would be a perfect sphere in three dimensions. But in reality, the microphone gets in the way of the incoming sound when the membrane is pointing away from the sound source. Therefore, the sphere would be flattened somewhat in this direction. The bi-directional polar pattern shown in Figure 4 would be indicative of a microphone that receives sound energy from both the front and the back of the membrane but rejects sound from the sides.

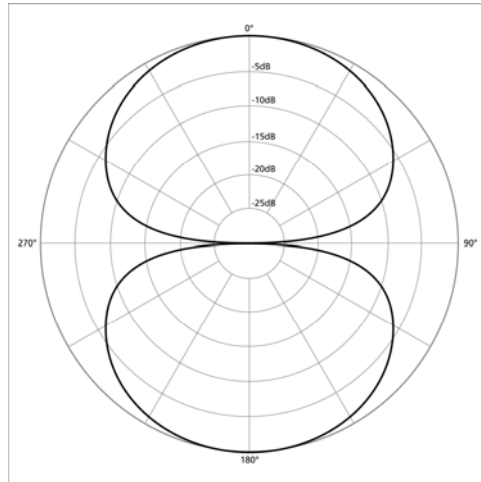


Figure 4. Bi-directional polar pattern [From 15]

The cardioid polar pattern, as shown in Figure 5, is also called a unidirectional pattern. This type of pattern is indicative of a microphone that would pick up sound from the front but reject sound from behind the microphone.

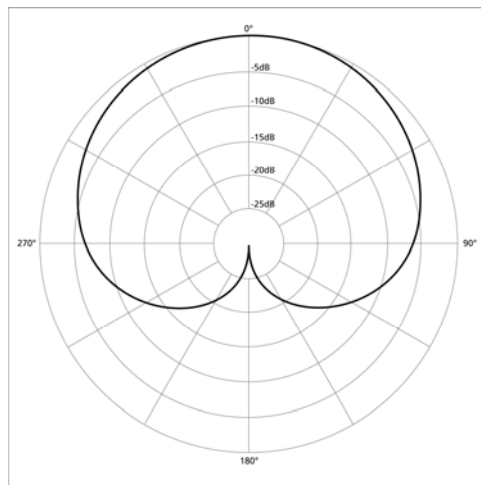


Figure 5. Cardioid polar pattern [From 15]

What actually determines the polar pattern is the internal structure of the microphone and whether or not the back side of the membrane is fully closed, partially closed or completely open to the environment. These patterns can also be achieved by adding the signal from an omnidirectional microphone to the signal from a bi-directional microphone. It is possible to achieve various polar patterns by adjusting the weighting of the aforementioned signals [16].

## **B. DYNAMIC PRESSURE MICROPHONE**

A dynamic pressure microphone makes use of a diaphragm that is situated between the external environment and a fixed volume of air. This type of microphone responds to the sound pressure that exists in front of its membrane. The membrane is displaced due to the pressure variations of the incident sound wave. The backside of the membrane must be acoustically separate from the front of the membrane as the fixed volume of air behind the membrane is crucial to the acoustic-mechanical coupling. Only a very small hole in the enclosed volume is necessary for equalization of barometric pressure. A pressure microphone is considered to be omnidirectional since it responds uniformly in all directions. As well, pressure is a scalar quantity and, therefore, has no direction associated with it.

The displacement of the membrane is dependent upon the force ( $F$ ) applied to it. Mathematically speaking,

$F = PA$  where  $P$  is the pressure at the membrane's surface and  $A$  is the area of the membrane.

The above is true as long as the dimensions of the membrane are small compared to the wavelength of the sound.

## **C. PRESSURE GRADIENT MICROPHONE**

A pressure gradient microphone employs a membrane that is at least partially open to the environment on both sides. The membrane is driven by the pressure difference or pressure gradient on the two sides of the membrane. A pressure gradient microphone is equally sensitive to sounds that arrive from the front side or the back side.

Sound waves that are parallel to the plane of the membrane do not produce a pressure difference between the two sides of the membrane and therefore a parallel sound wave does not displace the membrane. This type of microphone has a bi-directional, or figure eight polar pattern, as displayed in Figure 4. The physical shape of the microphone and any baffle enclosing the microphone can alter the microphone's directional response [17]. The pressure gradient microphone is sometimes called a particle velocity microphone because the output of the microphone is proportional to the air particle velocity.

#### D. PRESSURE GRADIENT MICROPHONE PHYSICS

Consider an acoustic wave incident on a small membrane of area  $S$  mounted on a finite baffle. Let the angle of incidence,  $\theta$ , be measured with respect to the normal to the membrane and baffle.

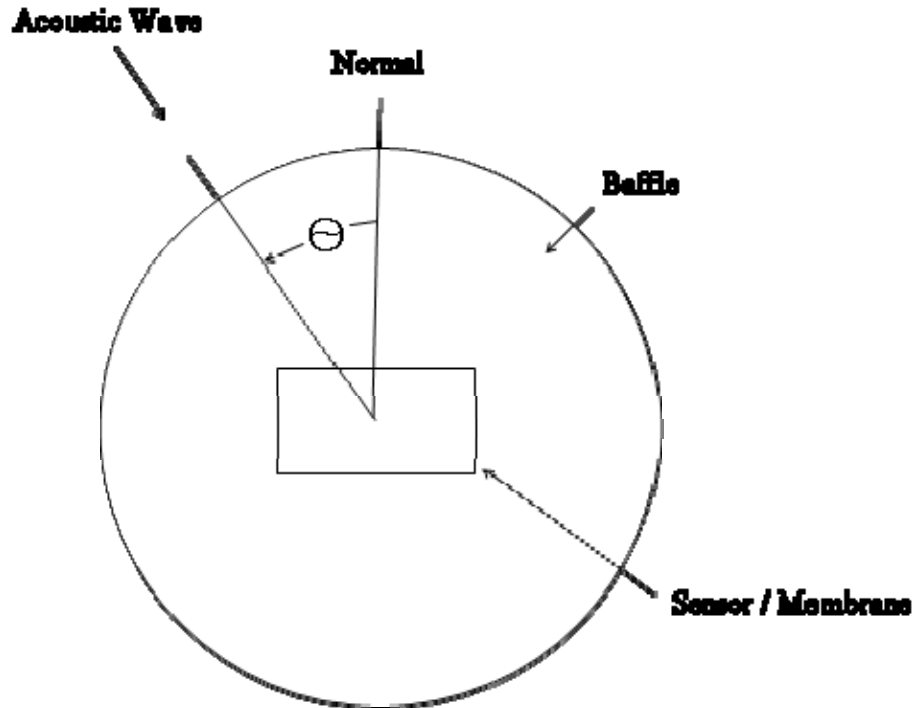


Figure 6. Acoustic wave incident on a small membrane with a finite baffle.

If the membrane has dimensions much less than the wavelength of the sound then the pressure,  $p(t)$ , on the front of the membrane can be written as

$$p(t) = p e^{j\omega t} \quad (3.1)$$

The amount of time,  $\tau$ , it takes for the pressure to be transmitted around the baffle to the back of the membrane is approximated as [18]

$$\tau = \frac{L}{c} \cos \theta, \quad (3.2)$$

where  $L$  is some effective travel path at normal incidence,  $c$  is the speed of sound in the medium, and  $\theta$  is the angle of incidence.

The net force  $F$  exerted on the membrane with area  $A$  is given by

$$F(t) = A[p(t) - p(t + \tau)] \quad (3.3)$$

Using Equation 3.2

$$F(t) = PA(1 - e^{jkL \cos \theta})e^{j\omega t} \quad (3.4)$$

where  $k = \frac{2\pi}{\lambda}$  is the wavenumber [18].

Further to the above, if we expand Equation 3.4,

$$F(t) = PAe^{j\omega t} e^{-\frac{j}{2}kL \cos \theta} \left[ e^{\frac{j}{2}kL \cos \theta} - e^{-\frac{j}{2}kL \cos \theta} \right] \quad (3.5)$$

$$F(t) = PAe^{j\omega t} e^{-\frac{j}{2}kL \cos \theta} 2j \sin\left(\frac{kL}{2} \cos \theta\right) \quad (3.6)$$

But  $kL \ll 1$ , and so, using the small angle approximation of  $\sin \theta \approx \theta$ ,

$$F(t) \approx PAe^{j\omega t} e^{-\frac{j}{2}kL \cos \theta} (kL \cos \theta) \quad (3.7)$$

$$= \tilde{F}_p e^{j\omega t} (kL \cos \theta) \quad (3.8)$$

The bending modal displacement of the plates can be represented by

$$\tilde{y}_{bend} = \frac{F(t)}{j\omega \tilde{Z}_{bend}} = \frac{\tilde{F}_p e^{j\omega t}}{j\omega \tilde{Z}_{bend}} (jkL \cos \theta) \quad (3.9)$$

where  $\tilde{Z}_{bend}$  is the “modal” mechanical impedance for bending motion.

Similarly, one may develop further understanding of the rocking motion and angle of incidence. The rocking motion is driven by a combination of pressure difference between the front and back of the sensor, and the pressure difference along the longitudinal axis of the two plates. This results in a planar quadrapolar directional response ( $\sin 2\theta$ ). The rocking modal displacement of the plates can be represented by

$$\tilde{y}_{rock} = \frac{\tilde{F}_p e^{j\omega t}}{j\omega \tilde{Z}_{rock}} (j k L \cos \theta) (j k d \sin \theta), \quad (3.10)$$

where  $\tilde{Z}_{rock}$  is the modal mechanical impedance for rocking motion, and  $d$  characterizes the longitudinal separation distance between the two plates. It is not simply their center-to-center separation because the plates are cantilevered, but it must be comparable to this distance.

By the symmetries of the motion for each mode, bending and rocking, the motion of each plate can be written as

$$\tilde{y}_{plate} = \tilde{y}_{bend} + \tilde{y}_{rock} \quad (3.11)$$

The contribution, both magnitude and phase, of each mode to the motion of each plate is frequency dependent, through  $\tilde{Z}_{bend}$  and  $\tilde{Z}_{rock}$ , and angular dependent. In later analysis of plate motion, it will be convenient to represent this for one plate as

$$\tilde{y}_{plate} = \tilde{a}_{bend} \cos \theta + \tilde{a}_{rock} \sin(2\theta) \quad (3.12)$$

## **IV. MODELING AND SIMULATION**

### **A. OVERVIEW**

A model is a simplified representation of the system under investigation. A simulation refers to the computer model and boundary conditions set upon it which is examined with various inputs. Whether or not the model represents reality depends on several factors. If the model is too simple then it does not promote understanding of the problem being investigated. On the other hand, if the model is too complex then it can hamper understanding due to the long computing time required. A software model that has results that are in the same vicinity as experimental data lead to deeper understanding of the problem and confirm that the model represents reality. A successful model can help to defray the costs of research and development, especially when the cost of fabrication is expensive. Previous work by NPS Students Shivok, Dristas and Chatzopoulos laid the foundation work for this thesis. As in their theses, the software package used to build the model and simulate the response of the MEMS microphone was COMSOL Multiphysics. The initial aim of this work was to reproduce the work performed earlier to ensure that the model and all parameters were entered correctly. Following successful trial runs, several iterations of optimization were performed on the model to reduce the necessary simulation time per frequency. These optimization techniques included altering the modeled volume, creating a symmetry plane, optimizing the mesh, and removing the perfectly matched layer (PML) used for sound absorption. Finally, a model including the substrate was constructed to simulate a more realistic situation. The data obtained showed an increase in response amplitude and led to further understanding of the MEMS microphone.

#### **1. System Requirements**

The sheer volume of calculations required for simulating the MEMS microphone required state of the art computational power in a desktop computer. The computer used for the modeling and simulation was a Dell Precision T7400. It is a Quad-Core Intel Xeon Processor running at 3.00 GHz. The operating system is Microsoft Windows XP

Professional x64 Edition Version 2003 with Service Pack 2. Even with 8GB of RAM, the computer was only effective running one simulation at a time.

## **2. COMSOL Software**

### ***a. Overview***

The software package selected to model and simulate the microphone was COMSOL Multiphysics Version 3.5a [2]. It is a powerful interactive environment for solving problems based on partial differential equations. Multiphysics was selected because there was previous in-house experience and expertise regarding its use as well as confidence in its capabilities. Initially, a non-acoustic model of the MEMS microphone (with the incident sound field represented by an analytic expression) was constructed, as in previous theses. After successful implementation of the non-acoustic model, efforts were shifted to the implementation of an acoustic model by introducing the sound field.

The sound field will impart a force onto the sensor. This is in direct contrast to some of the previous work whereby the acoustic wave was simulated by approximating the acoustic wave with a force applied to the surface of the sensor. To couple the acoustic and solid structure domains within Multiphysics, the Acoustic module was selected for the acoustic domain and the MEMS module was selected for the structural domain. After much research and work following examples in the Multiphysics manuals regarding how to couple the solid and fluid domains, a more efficient module was selected, which was the Acoustic-Structure Interaction module. This module allows the user to couple the acoustical and structural domains by selecting which elements are of the fluid domain and which are of the solid domain. As well, boundary conditions can be applied and coupling equations are automatically established.

***b. Model Entry and Simulation Procedure***

There are several steps that one must follow to ensure the model is entered into Multiphysics correctly. The major steps required for model entry and simulation are:

- i. choose application mode;
- ii. generate 2D representation of model;
- iii. extrude 3D representation of model;
- iv. define subdomains;
- v. select boundary conditions;
- vi. create finite element mesh, and
- vii. select solver parameters.

These steps will be covered in detail in later chapters.

**B. NON-ACOUSTIC SIMULATIONS**

**1. Model Construction**

One sensor from the 4<sup>th</sup> generation design was used in a non-acoustic simulation in order to get a baseline for comparison purposes. The application mode selected was the MEMS module -> Structural Mechanics -> Solid Stress-Strain. The initial step is to enter the model geometry in 2D and then extrude it into 3D. The 2D model is shown in Figure 7.



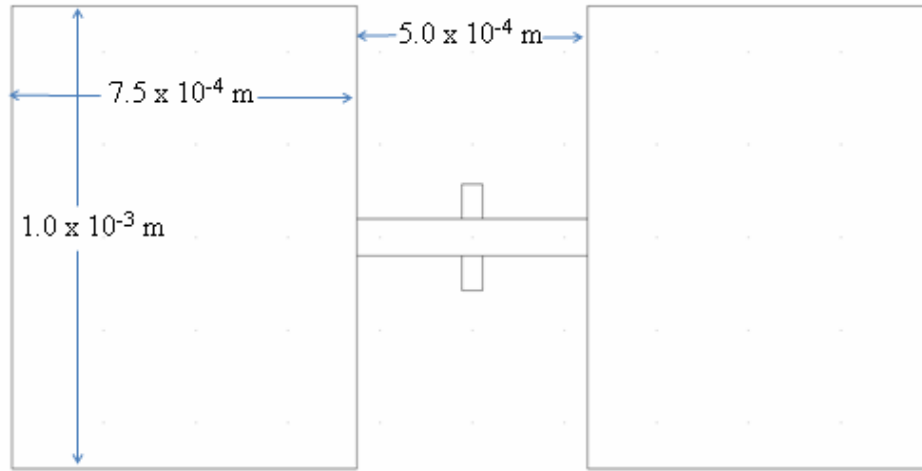


Figure 7. 2D view of the 4<sup>th</sup> generation sensor used for simulation.

The 2D model is then extruded to the desired thickness (10  $\mu\text{m}$ ) and the result is shown in Figure 8.

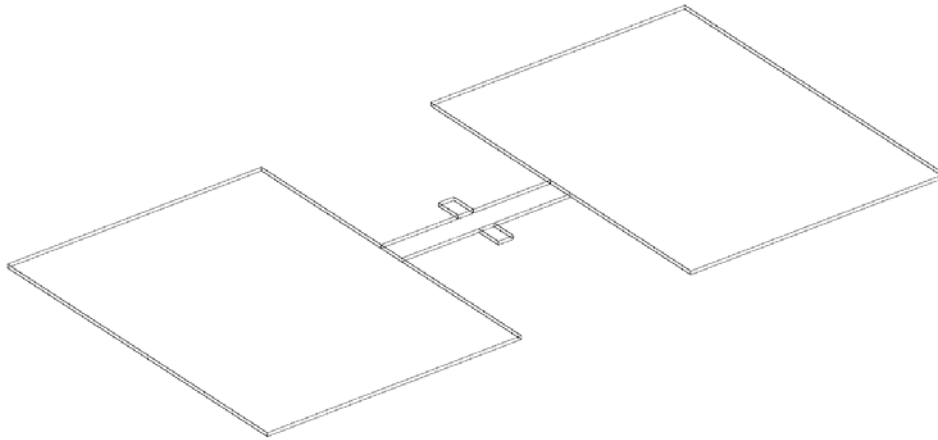


Figure 8. 3D model of the sensor in Figure 7.

The next step in the process is to define the subdomain(s) comprising the object(s) being modeled. Each subdomain may be selected as active or inactive within each physics application mode. The properties of each subdomain within each application mode are then selected and boundary conditions are specified, as required.

As in previous non-acoustic simulations, the acoustic wave was introduced into the simulation as a force directed on the upper side of the sensor plates. The force was calculated

analytically within Multiphysics by integrating the pressure over the surface of each plate [11]. A damping due to air was introduced on the bottom face of the sensor wings by estimating damping pressure following Zhang et. al [19]. Again, this information was used from [11], to ensure the results would be consistent with previous work. The formulae used for non-acoustic simulations are shown in Table 1.

Paramater	Value	Description
$\mu$	1.871e-5	Viscosity of the ambient air ( Pa sec)
$\theta$	Any value from 0 to 90	Incident angle (degrees)
$\phi$	$\omega * \tau * \frac{180}{\pi}$	Phase (degrees) where $\omega$ is the resonant angular frequency
$\tau$	$-x * \sin(\theta * \frac{\pi}{180}) \frac{1}{v_s}$	Time difference (seconds) where $v_s$ is the speed of sound in ambient air
pda	$b\pi\sqrt{\frac{\rho\mu\omega}{2}}v_{z-direction}$	Formula computing air damping pressure [19]
$b$	2	Empirical dimensional parameter [19]
$\rho$	1.25	Ambient air density (kg/m <sup>3</sup> )

Table 1. Parameters used for non-acoustic COMSOL simulations [From 11].

The sensor was made of silicon and thus the solid subdomain was modeled by selecting Si and had the following properties associated with it.

Parameter	Value	Units
Young's Modulus	$170 \times 10^9$	$Pa$
Poisson's Ratio	0.28	
Density	2329	$\frac{kg}{m^3}$

Table 2. Silicon subdomain properties.

Figures 9 and 10 show the boundary condition parameters as they are set for the top and bottom of the plates, respectively. The sound pressure amplitude of 1 [Pa] on the top plate with a linear phase change across the surface,  $\phi$ , were implemented in Multiphysics. The damping force exerted on the bottom plate is in the opposite direction to the velocity of the plate, and is represented in Table 1 by pda.

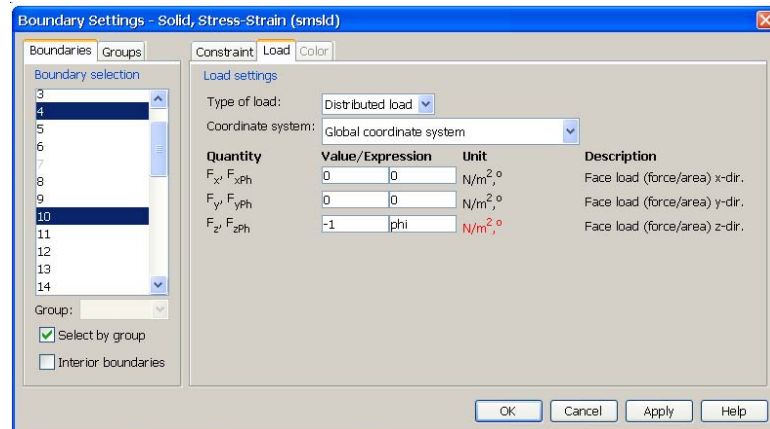


Figure 9. Incident pressure applied on top side of plates.

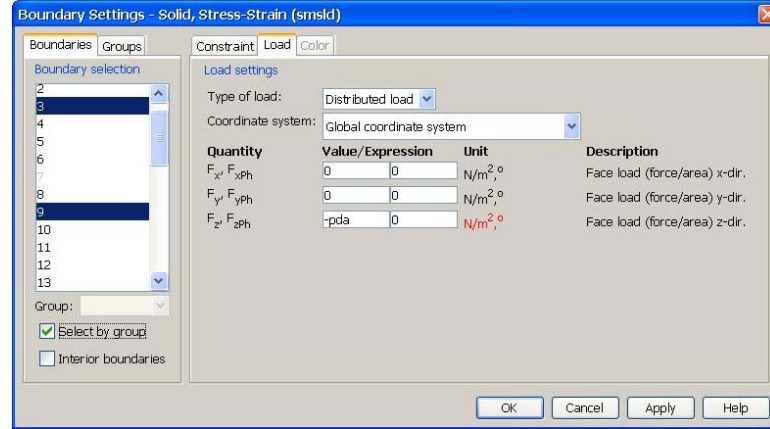


Figure 10. Air damping pressure applied on bottom side of plates.

In addition to the previous boundary conditions, the middle section of the sensor must be fixed to represent how the sensor would be attached to its substrate.

After the boundary conditions are applied then a finite element mesh must be generated for each subdomain. The results of the meshing are shown in Figure 11.

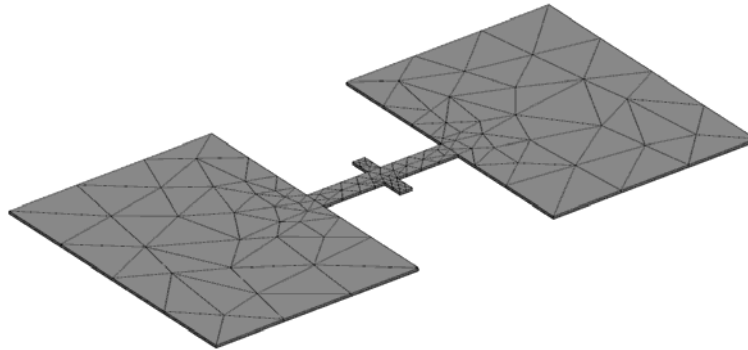


Figure 11. Finite element mesh used for simulation.

Finally, the solver parameters must be selected including the mathematical solver and the frequency range. The selection of the mathematical solver is transparent to the user. However, entry of appropriate frequencies and frequency ranges is vital to achieving a thorough solution for the simulation.

The simulation results obtained were consistent with previous non-acoustic simulations. The first two resonant frequencies or normal modes of oscillation were a rocking mode and a bending mode. These modes are illustrated in Figures 12 and 13 below.

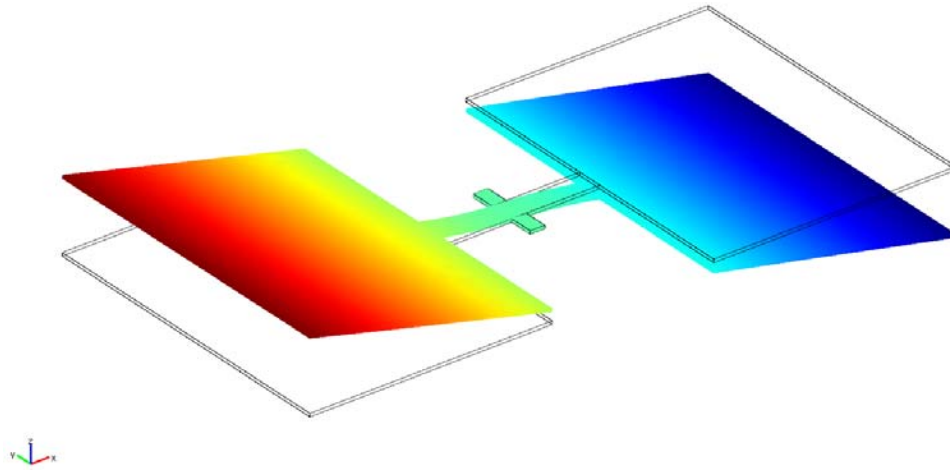


Figure 12. Rocking mode at 3,573 Hz.

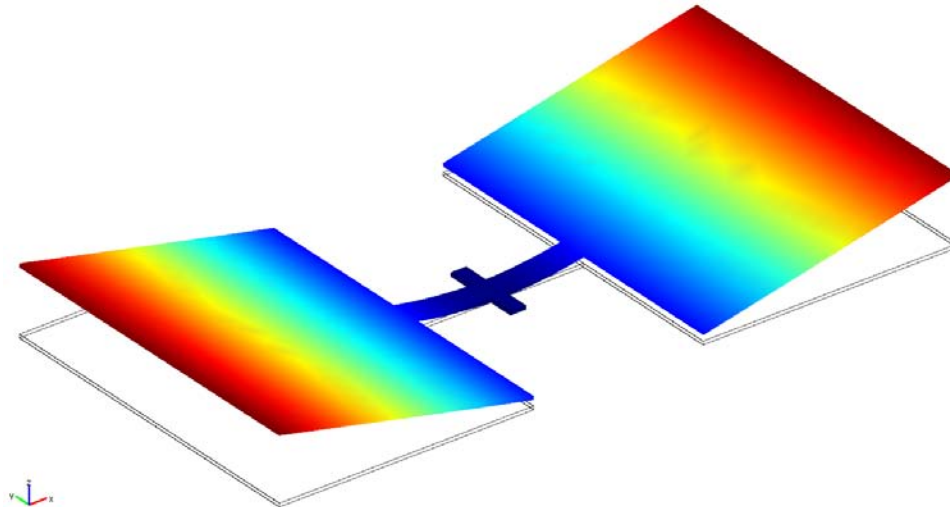


Figure 13. Bending mode at 4,013 Hz.

The results of several simulation runs for various angles of incidence appear in Table 3. All simulations resulted in a rocking frequency of 3,573 Hz and a bending frequency of 4,013 Hz. The ipsilateral plate displacement (plate closest to the sound

source) is larger than the contralateral plate displacement (plate furthest from the sound source), which is the case for all angles of incidence around the resonant frequencies. The ipsilateral plate amplitude of the rocking mode increases as the angle of incidence increases. However, the amplitude of the bending mode remains constant while varying the angle of incidence.

Angle of Incidence (degrees)	Plate Displacement (nm)			
	At Rocking Frequency		At Bending Frequency	
	Ipsilateral	Contralateral	Ipsilateral	Contralateral
10	672	302	19170	19080
20	850	125	19170	19080
30	1016	52	19170	19080
40	1167	199	19170	19080
50	1297	329	19170	19080
60	1402	435	19170	19080
70	1480	513	19170	19080
80	1528	560	19170	19080
90	1544	576	19170	19080

Table 3. Non-Acoustic multiphysics simulation of amplitude of oscillations at rocking and bending frequencies for a 1 Pa incident plane sound wave.

Although these initial steps were not absolutely necessary, it gave the author time to become familiar with the Multiphysics code and to gain confidence in the simulation results. The frequency response of the non-acoustic model is shown in Figures 14 and 15 at a 45-degree angle of incidence. The smaller amplitude at the rocking frequency is expected since it is driven by the sound pressure difference between the two wings. It can be seen that the amplitudes of vibration on the ipsilateral and contralateral sides are different due to the effect of the superposition of the two modes at the rocking frequency.

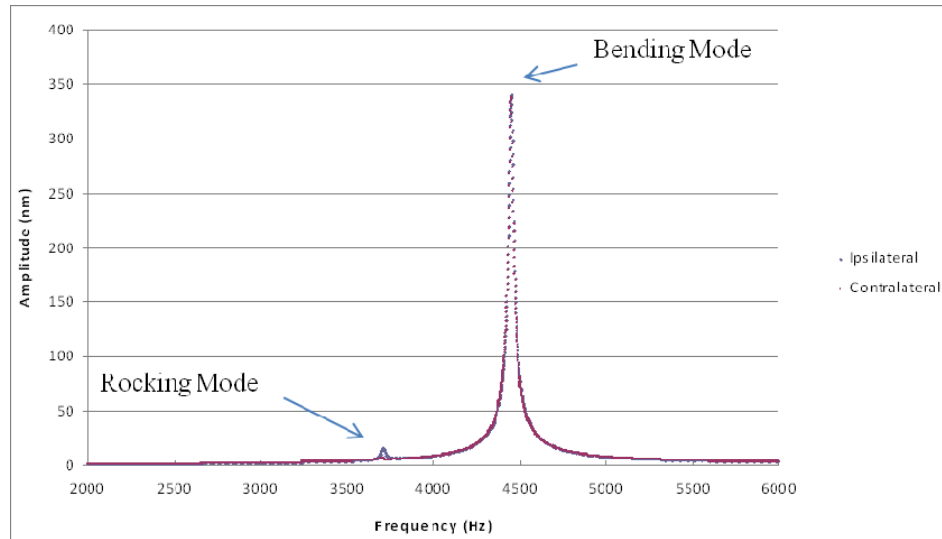


Figure 14. Non-Acoustic broadband frequency response at 45-degree angle of incidence.

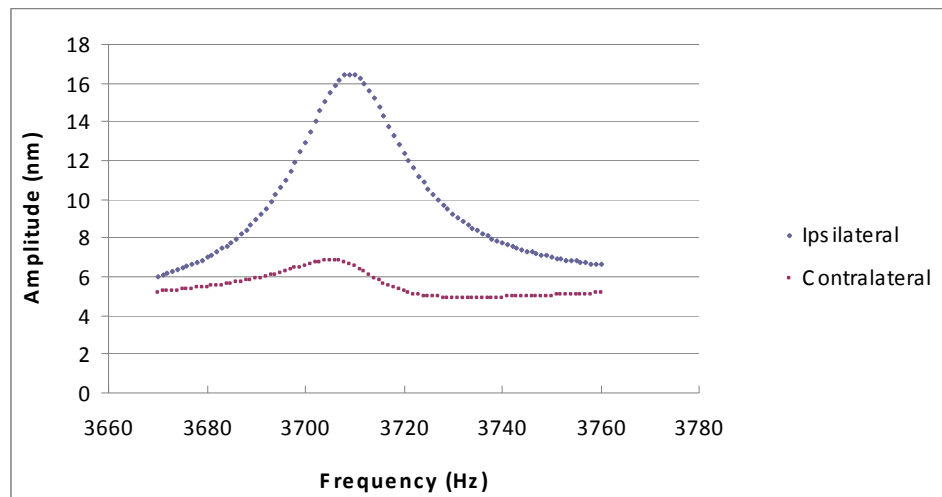


Figure 15. Non-Acoustic rocking frequency response at 45-degree angle of incidence.

## C. ACOUSTIC/STRUCTURE COUPLED SIMULATIONS

### 1. Model Construction

Once again, the construction of the sensor model was taken from the 4<sup>th</sup> generation 3D sensor, shown in Figure 7. Initially, the application mode selected was the Acoustic-Structure interaction, as shown in Figure 16.

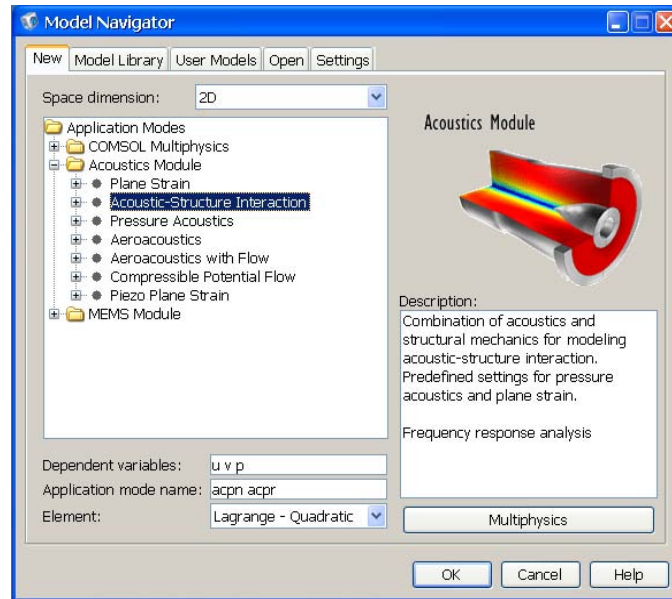


Figure 16. Acoustic-Structure interaction application mode.

There were two subdomains in this model, solid and fluid. The acoustic (fluid) subdomain was modeled as a spherical volume, and was used to encompass the sensor. This volume was in turn enclosed by another spherical volume that acted as a perfectly matched layer (PML.) The PML was used to absorb acoustic energy, to simulate a free field effect, thereby eliminating acoustic energy being reflected back into the spherical volume from the sphere's outer shell. In addition, a radiation condition was applied to the outer spherical boundary, to assist in damping acoustic energy. The acoustic subdomain was modeled as air with a density of  $1.25 \text{ kg/m}^3$  and a speed of sound of  $343 \text{ m/s}$ . The solid subdomain was again modeled as Si with the same properties as previously mentioned in Table 2.

The device within the spherical volume is shown at Figure 17.



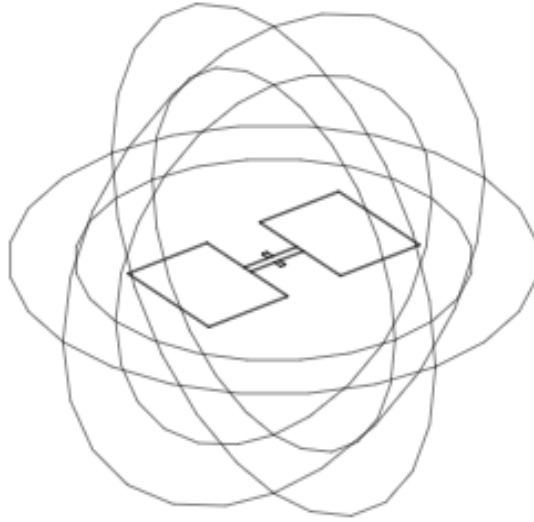


Figure 17. 3D acoustic volume with perfectly matched layer and the sensor at the center.

The next step after the subdomains are entered is to enter the boundary conditions. Each physics mode, pressure acoustics and solid stress-strain, must be selected and the appropriate boundary conditions must be applied to each boundary. Typical boundary conditions for pressure acoustics included radiation condition, sound hard boundary, and structural acceleration. Typical boundary conditions for the solid, stress-strain module included x-z symmetry plane, fixed, fluid load, and fluid load with damping.

After successful entry of boundary conditions, meshing of the entire structure must be carried out. The most vital section to be meshed for this model was the middle portion of the sensor between the two plates. The smaller the mesh in this area, the more accurate the resonant frequencies.

Finally, the solver parameters must be entered. Selection of the type of solver as well as a range of frequencies to solve for may be entered. Typically, the range of frequencies was from 2,000 to 6,000 Hz for the present sensor and was broken down into various regions. A smaller frequency increment was used in critical areas around the rocking and bending frequencies.

The source of the plane wave was a scalar variable entered under Physics -> Scalar Variables,  $p_{i\_acpr}$ , which was introduced into the model by the following equation:

$$\text{Incident Acoustic Pressure} = e^{[-ik_{acpr}(x\cos\theta - z\sin\theta)]} \quad (4.1)$$

Where  $k_{acpr}$  is the wave number,  $\theta$  is the angle of incidence and  $x$  and  $z$  are the Cartesian coordinates. Equation 4.1 represents a plane wave and the resultant pressure fluctuations are shown in Figure 18. The frequency was altered to 200 kHz for demonstration purposes.

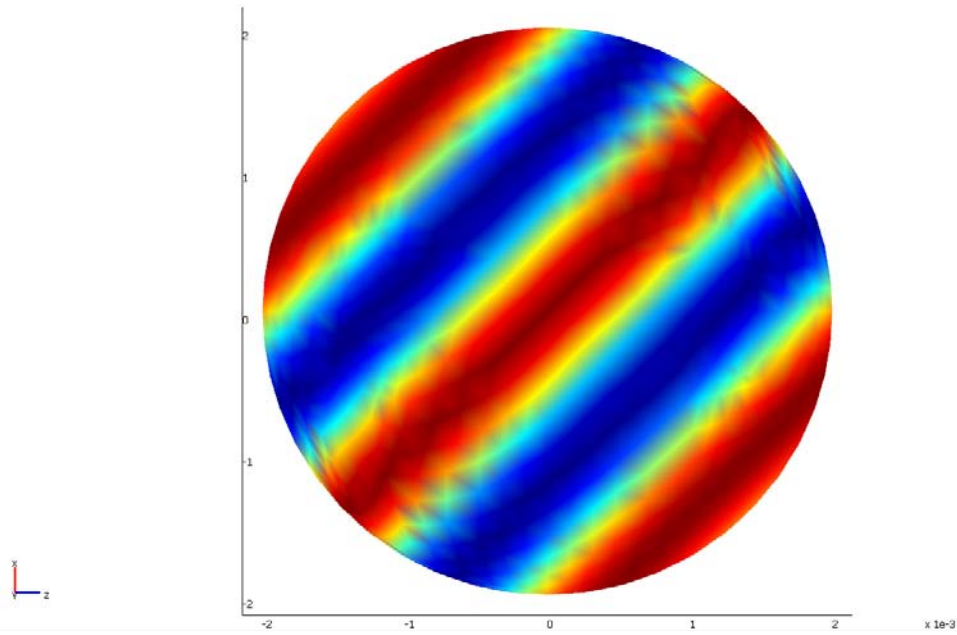


Figure 18. Plot of incident plane wave in multiphysics at 200 kHz.

There is one important assumption and one important constraint regarding the acoustic wave. First, by introducing the wave as a plane wave, the model assumes that the sensor is at a range that would be far enough from the sound source to be considered to be in the far field. As you can see by Equation 4.1, the acoustic wave is only introduced in two dimensions,  $x$  and  $z$ . Therefore, the source is constrained to lie in the  $x$ - $z$  plane. This constraint was not necessary at this stage but was vital during the optimization phase that will be discussed later.

The same damping pressure was used for the backside of the sensor as shown in Table 1. In the non-acoustic model, where the acoustic module was not included in the application mode selection, the variables used by Multiphysics contain the first two letters of the mode selected, i.e., sm. However, when two physics application modes are used then the user must ensure that the damping equation contains the variable name corresponding to the correct physics module and variable within that module. Therefore, for this model, the names of variables within the damping pressure equation had to be changed to ensure the correct variables were used. Selection of the correct variable ensured proper coupling of the acoustic and solid subdomains. The changes to the air damping equation were

$$\omega\_smsld \rightarrow \omega\_acsld$$

and

$$w\_t\_smsld \rightarrow w\_t\_acsld .$$

This model worked extremely well. The results obtained not only confirmed findings from previous theses but also contradicted some previously reported results. The acoustic model simulation obtained the same first two modes of oscillation (rocking and bending) and confirmed that the response amplitude of the ipsilateral plate is slightly greater than the contralateral plate. However, the most unique finding of the acoustic model simulation was that the bending mode amplitude was not constant for various angles of incidence, contrary to simulations as reported in [11]. As well, the rocking mode amplitude maximum occurred at a 40 degree angle of incidence rather than a 90 degree angle of incidence as was previously reported. Figure 19 shows the simulated bending mode amplitude (normalized) as a function of incident angle of sound and Figure 20 shows the experimental data obtained by LCDR M. Touse [20]. The results obtained were in good agreement with experimental data collected by LCDR M. Touse.

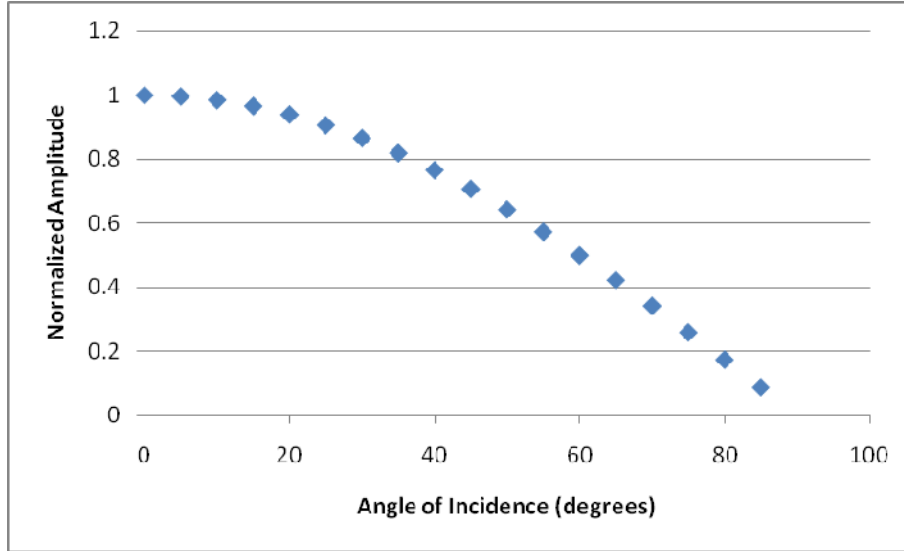


Figure 19. Simulated amplitude at bending frequency.

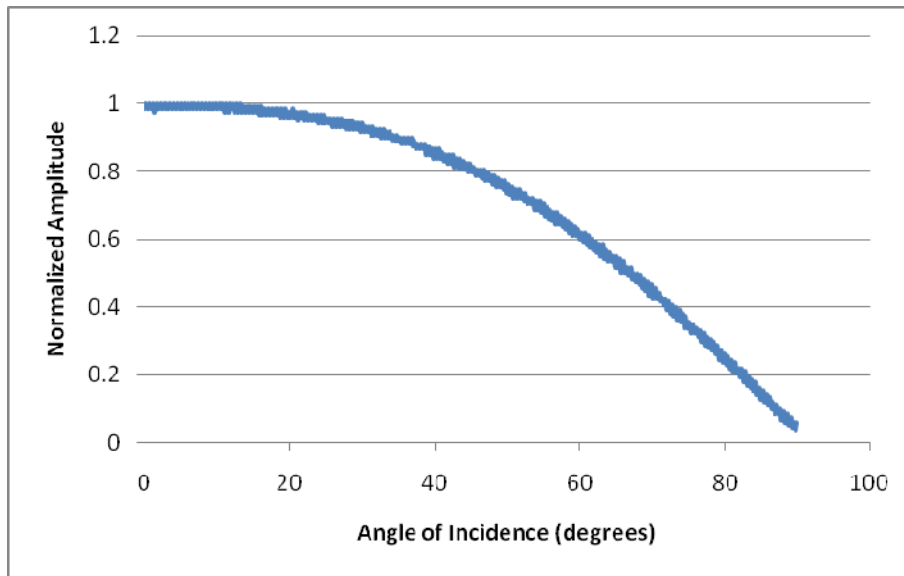


Figure 20. Measured amplitude at bending frequency [From 20].

## 2. Finite-element Model Optimization

Reference [11] created a model with a sound point source but at a huge computational cost. The computation time was on the order of days to compute a solution. This thesis has not only introduced the acoustic/structure interaction but has done so in a very efficient manner in regards to computation time. Initial acoustic interaction resulted in a run time of 100 seconds per frequency. The key to this relatively

fast computation time was the way in which the acoustic wave was introduced into the model as a scalar function. This section describes further optimization that was done to reduce the computation time. Various optimization techniques allowed Multiphysics to compute a solution in a time of 12 seconds per frequency.

***a. Spherical Volume 3D Model***

Initially, with no optimization of the model, the simulation, as modeled in Figure 17, took approximately 100 seconds per frequency to develop a solution. This 100-second solution is based upon a spherical volume with a PML. Of course, the solution depends on various factors within Multiphysics, namely, the size of mesh. The smaller the mesh elements, the greater the number of elements required in a volume and therefore, the longer the solution time. In this stage of development the meshing used was similar in size to that used for the non-acoustic model as shown in Figure 11.

***b. Hemispherical Volume***

The first step of optimization introduced was to attempt to eliminate one half of the model due to the symmetric nature of the sensor and the desired solution for the motion and the acoustic field. It was decided that a hemisphere would be the natural optimization volume since the model could easily be cut in half. The model was redrawn and is shown in Figure 21.

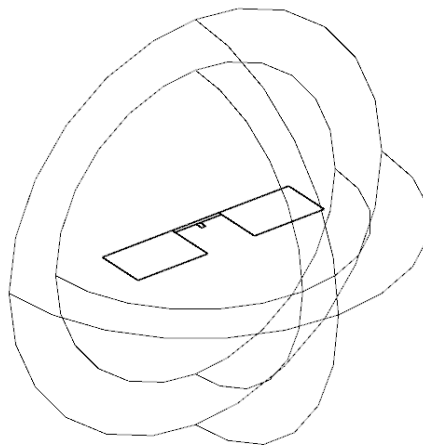


Figure 21. Hemispherical acoustic subdomain.

It can be seen in Figure 21 that one half of the sensor and one half of the spherical volume were removed. This resulted in a decrease in the solution time to approximately 50 seconds per frequency. This was easily achievable because Multiphysics allows the user to set up a symmetry plane.

*c. Cylindrical Volume*

The second step was to try to change the acoustic domain into a smaller volume by changing the existing hemispherical volume into a cylindrical volume while at the same time maintaining the symmetry condition. This resulted in a decrease in the volume thereby reducing the number of finite elements that in turn resulted in a decrease in the solution time. The cylindrical volume with sensor can be seen in Figure 22.

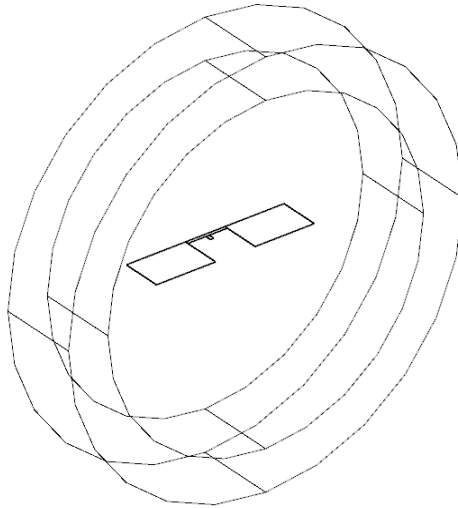


Figure 22. Cylindrical acoustic subdomain.

*d. Meshing*

Meshing is by far the most important factor in optimizing solution time. The model can be broken down into several subdomain volumes to examine the effects of meshing on both the solution and the computation time required. These volumes included the sensor middle section, sensor wings or plates, air volume and perfectly-matched layer (PML), as shown in Figure 23.

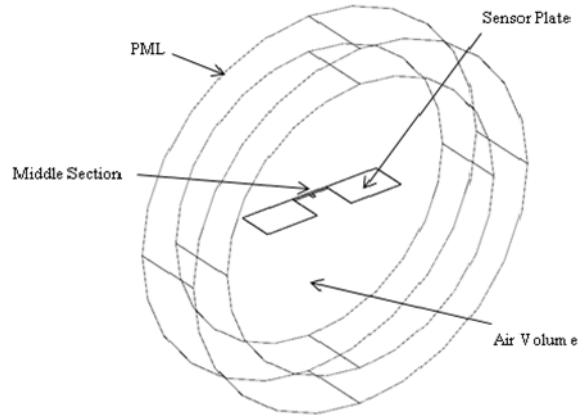


Figure 23. Subdomains used for meshing.

Initially, a baseline run was conducted with the smallest mesh that would allow the computer to calculate a solution without receiving an out of memory error. This run took over 48 hours to achieve a solution and was considered to be the most accurate numerical solution to this problem. A series of simulations with various mesh configurations were built. Solutions were calculated for these models to determine which configuration would have the optimal solution. The optimal solution selected had a combination of the resonant frequency and amplitude that was near the baseline frequency. As well, the optimal solution had a relatively short computation time per frequency. A sample of the results of several meshing configurations can be viewed in Table 4.

<b>Mesh Configuration</b>	<b>Leg/Mid</b>	<b>Wings</b>	<b>PML</b>	<b>Air</b>	<b>Frequency (Hz)</b>	<b>Amplitude (nm)</b>	<b>Sec/Freq</b>
Baseline	Extremely Fine	Normal	Extra Fine	Normal	4419	349	165.2
1	Coarser	Extremely Coarse	Normal	Normal	4487.5	339	7.9
6	Coarser	Extremely Coarse	Fine	Normal	4488	339	8.0
8	Coarser	Extremely Coarse	Extra Fine	Normal	4487	339	12.0
10	Coarse	Extremely Coarse	Extremely Coarse	Normal	4484	335	8.1
16	Coarse	Extremely Coarse	Finer	Normal	4484	335	12.1
20	Extremely Fine	Extremely Coarse	Normal	Normal	4452	339	15.0
22	Extremely Fine	Coarser	Normal	Normal	4424	347	39.2
24	Finer	Coarser	Normal	Normal	4428	346	38.0
25	Extremely Fine	Coarse	Normal	Normal	4421	348	390.9
27	Extra Fine	Extremely Coarse	Extremely Coarse	Normal	4454	340	13.1
31	Extra Fine	Normal	Extremely Coarse	Normal	4422	349	264.3
32	Finer	Extremely Coarse	Normal	Normal	4449	340	12.8
37	Fine	Extremely Coarse	Normal	Normal	4462	338	9.9
42	Normal	Extremely Coarse	Normal	Normal	4480	335	8.9
47	Coarse	Extremely Coarse	Normal	Normal	4484	338	8.6
52	Coarser	Extremely Coarse	Normal	Normal	4488	339	7.8
57	Extra Coarse	Extremely Coarse	Normal	Normal	4561	334	6.3
62	Extremely Coarse	Extremely Coarse	Normal	Normal	4660	367	5.7

Table 4. Mesh configuration and best compromise for optimization of mesh.

It was decided that mesh configuration 32 would be used for the remainder of this thesis as it was the best compromise of the three factors: frequency delta, amplitude delta and the number of seconds required per frequency to achieve a solution. The frequency delta was 30 Hz (0.7%). The amplitude delta was 9 nm (2.6%). The time



per frequency was 12.8 sec/Hz (7.7%.) This allowed for a reasonable solution in a practical timeframe allowing an abundance of future simulation runs to examine further optimization techniques.

*e. Change of Volume*

The next step in reducing the computation time was to examine the possibility of reducing the size of the cylindrical volume of the acoustic domain. The problem was broken down into several steps. First, the thickness of the cylinder was reduced to determine what effect, if any, this would have on the solution. Results are shown in Table 5.

<b>Thickness (mm)</b>	<b>Bending Frequency (Hz)</b>	<b>Ipsilateral Amplitude (nm)</b>	<b>Contralateral Amplitude (nm)</b>	<b>Sec/Freq (s/Hz)</b>	<b>Degrees of Freedom</b>
5	4449	339	338	11.9	38613
4	4449	339	338	11.8	3826
3	4449	340	338	11.6	37459
2	4449	339	338	11.1	36484
1	4450	338	337	10.1	36754
0.8	4450	334	333	10.9	37994
0.6	4452	322	321	12.0	40964

Table 5. Effects of reduction of thickness of cylinder used for acoustic domain.

A thickness smaller than 2 mm resulted in a decreased amplitude response. Therefore, 2 mm was selected as the minimum thickness for the cylindrical volume.

Second, the radii of the inner and outer cylinders were changed to determine what effect this would have on the solution. The results are shown below in Table 6.

<b>Outer and Inner Radii (cm)</b>	<b>Bending Frequency (Hz)</b>	<b>Ipsilateral Amplitude (nm)</b>	<b>Contralateral Amplitude (nm)</b>	<b>Sec/Freq (s/Hz)</b>	<b>Degrees of Freedom</b>
2.0 / 1.5	4451	339	338	11.9	38613
1.75 / 1.3	4452	339	337	11.4	38456
1.5 / 1.1	4450	339	337	12.2	38305
1.25 / 0.94	4451	340	338	12.0	39365
1.0 / 0.75	4450	339	336	11.9	39892
0.75 / 0.56	4451	339	338	12.6	41314
0.5 / 0.38	4451	339	337	13.6	44049
0.25 / 0.19	4451	337	335	16.9	51238
0.15 / 0.11	4455	317	315	12.2	38582

Table 6. Effects of change in cylinder radii.

An outer radius of 1 cm resulted in comparable amplitude while having the lowest time per frequency needed for simulation.

*f. Perfectly Matched Layer*

The PML was eliminated without changing the radiation condition on the outside boundary to determine if this would have any impact on the solution. The data for various runs with a 1 cm radius and no PML are shown below in Table 7.

<b>Thickness (mm)</b>	<b>Bending Frequency (Hz)</b>	<b>Ipsilateral Amplitude (nm)</b>	<b>Contralateral Amplitude (nm)</b>	<b>Sec/Freq (s/Hz)</b>	<b>Degrees of Freedom</b>
5	4451	340	337	11.1	39759
4	4451	340	337	10.7	39225
3	4451	340	338	9.6	37627
2	4451	340	338	11.3	36692
1	4452	339	337	10.3	35112
0.8	4452	335	332	9.7	34082
0.6	4454	326	324	9.1	33703

Table 7. Effects of removal of perfectly matched layer in simulations.

The removal of the PML showed no appreciable difference for the simulation results. This indicates that the radiation boundary conditions used for the outer surface of the cylinder adequately absorb the incident sound wave. The removal of the PML resulted in no appreciable change to the amplitude nor the computation time but resulted in a small simplification to the model.

**3. Angle of Incidence**

All previous simulations were run with the incoming acoustic wave at a 45-degree angle of incidence to the sensor. The angle of incidence was varied to get an appreciation

of how the angle of incidence affects the amplitude of plate motion. The angle is measured from the normal to the surface of the sensor. So an angle of incidence of 0 degrees is normal to the sensor.

The amplitude of the ipsilateral plate at the rocking frequency versus the angle of incidence is shown in Figure 24. Also displayed in Figure 24 is the normalized best-fit versus expected ipsilateral plate amplitude as a result of the contribution from both the rocking and bending modes. A physical explanation of the model curve that was used to fit the data follows. It was found that the fraction of the plate motion due to rocking was 61%, and the fraction due to bending was 39%.

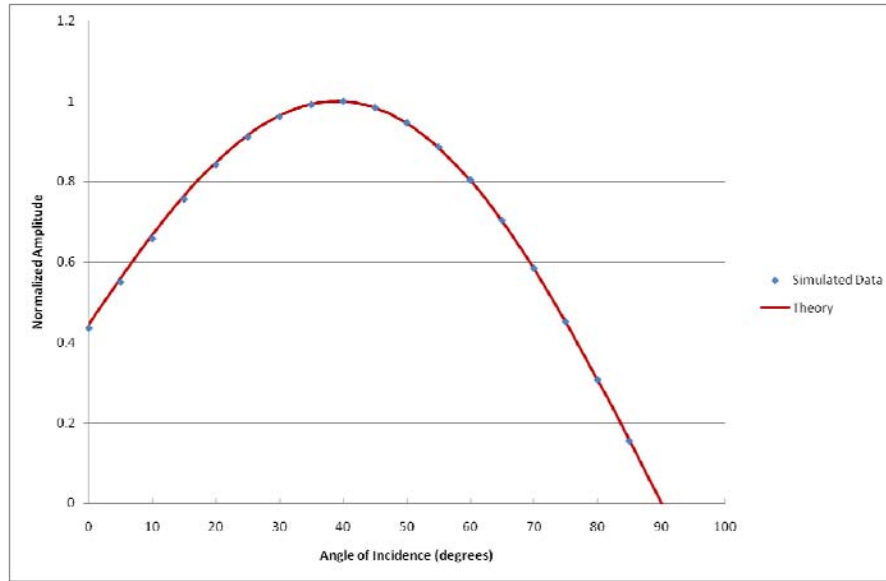


Figure 24. Simulated amplitude and best-fit amplitude of the ipsilateral plate at the rocking frequency as a function of incident angle

It is important to note that the maximum rocking amplitude occurs at an angle of incidence of approximately 40 degrees. This contradicts previous simulations [11] whereby the maximum rocking amplitude was reported at 90 degrees.

Both the bending and the rocking mode contribute to the amplitude of the response. An analytical model for the motion of a single plate was developed in Equations 3.9–3.12. Equation 3.12 is repeated here

$$\tilde{y}_{plate} = \tilde{a}_{bend} \cos \theta + \tilde{a}_{rock} \sin(2\theta). \quad (3.12)$$

The contributions to plate motion by each mode are represented by the coefficients  $\tilde{a}_{bend}$  and  $\tilde{a}_{rock}$ . Their amplitudes and phases have inherent contributions due to their dipolar or quadrupolar nature (the factors of  $jkL \cos \theta$  and  $jkL \sin \theta$  in equations 3.9 and 3.10.) Additionally, the amplitude and phase of each depends upon its modal impedance amplitude and phase.

As the driving frequency used to compute the simulated ipsilateral plate response shown in Figure 24 was the rocking modal frequency, the rocking modal impedance  $\tilde{Z}_{rock}$  is resistance-controlled, i.e., real-valued, whereas the bending modal impedance  $\tilde{Z}_{bend}$  is stiffness-controlled, i.e., imaginary-valued. This 90-degree phase difference in modal impedances cancels the inherent 90-degree phase difference in the dipolar versus quadrupolar responses, all else being equal. Accordingly, for this driving frequency, the bending and rocking mode contributions to the ipsilateral plate response should be in phase, and so the plate motion should be able to be modeled as

$$\tilde{y}_{plate} = a \cos \theta + (1 - a) \sin(2\theta), \quad (4.2)$$

where the real-valued parameter  $a$  is the fractional plate motion due to bending and  $(1-a)$  is the fractional plate motion due to rocking. This worked extremely well. A best-fit value of  $a$  was found to be 0.39.

That the ipsilateral plate motion at the rocking mode frequency should arise from almost equal parts rocking and bending is reasonable, as can be gleaned from Figure 14. It can be seen in Figure 14 that, at the driving frequency of the rocking mode, for an incidence angle of 45 degrees ( $\cos \theta = \frac{1}{\sqrt{2}}$ ,  $\sin 2\theta = 1$ ), the contribution to ipsilateral plate motion by the bending mode is comparable to that by the rocking mode. Incidentally, the converse is not true, that is, the contribution to ipsilateral plate motion at the driving frequency of the bending mode by rocking motion is negligible. This explains, for example, why no evidence of quadrupolar angular dependence is seen in Figure 19 or in Figure 25 (next section.)

#### D. INCLUSION OF SUBSTRATE

The next stage in investigating the acoustic model was to include some form of substrate surrounding the sensor to more realistically represent the fabricated sensor. A substrate size of 4mm x 1mm x 400 microns was used to determine how the inclusion of a substrate would impact the rocking and bending mode amplitudes. To perform this investigation, the angle of incidence of the incoming sound wave was varied from zero to 90 degrees. The meshing for this model was changed slightly from the previous simulations due to the inclusion of the substrate. The results are shown in Figure 25.

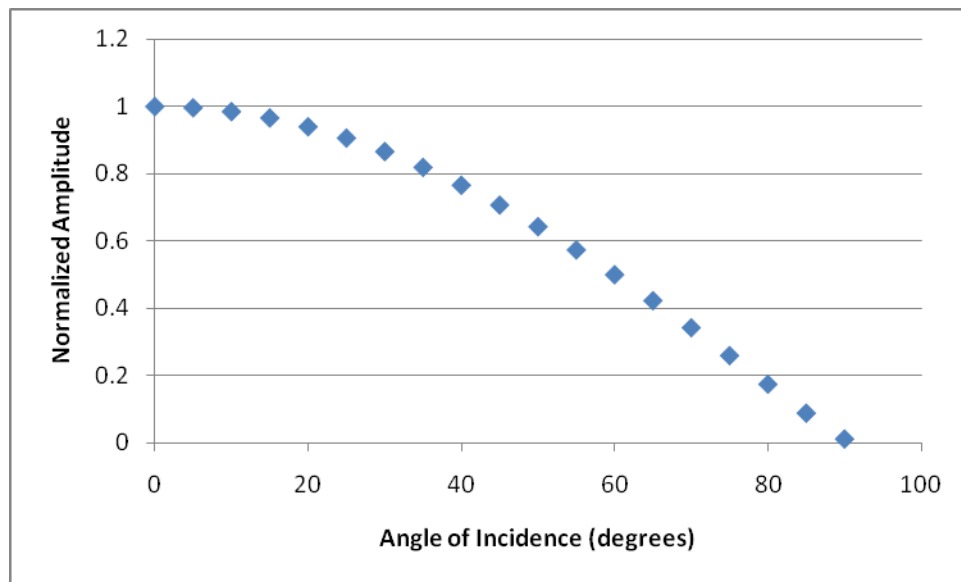


Figure 25. Simulated amplitude as function of incident angle at bending frequency including substrate surrounding the sensor.

It is significant to point out that the amplitude response actually increased with the introduction of the substrate, as illustrated in Table 8.

<b>Angle Of Incidence (degrees)</b>	<b>Ipsilateral Without Substrate (nm)</b>	<b>Ipsilateral With Substrate (nm)</b>
0	482	1118
5	480	1114
10	474	1101
15	465	1080
20	453	1051
25	437	1013
30	417	968
35	394	916
40	369	856
45	340	790
50	309	719
55	276	641
60	241	559
65	203	473
70	164	383
75	125	290
80	84	195
85	42	98
90	0	12

Table 8. Amplitude as a function of incident angle at bending frequency with and without substrate around the sensor.

This can be explained by examining the theory in Chapter III section D. By including the substrate, the length the acoustic wave must travel to reach the back side of the sensor is increased. This increased length results in a larger pressure gradient that in turn leads to increased amplitude. The maximum response would occur if the effective length were one half wavelength. This would result in maximum pressure gradient and maximum amplitude response. The effective length is approximately 3.5 cm at 5,000 Hz. For a sensor that is 2 mm x 1 mm, this effective length is not practical since the baffle must still be small as compared to  $kL$ . To investigate this, changes were made to the substrate size in stages to examine this relationship. First, the width and then the length of the substrate was changed to examine the amplitude response of each variation. Then both width and length were changed to examine this impact. Figures 26, 27 and 28 show the results of several simulation runs.

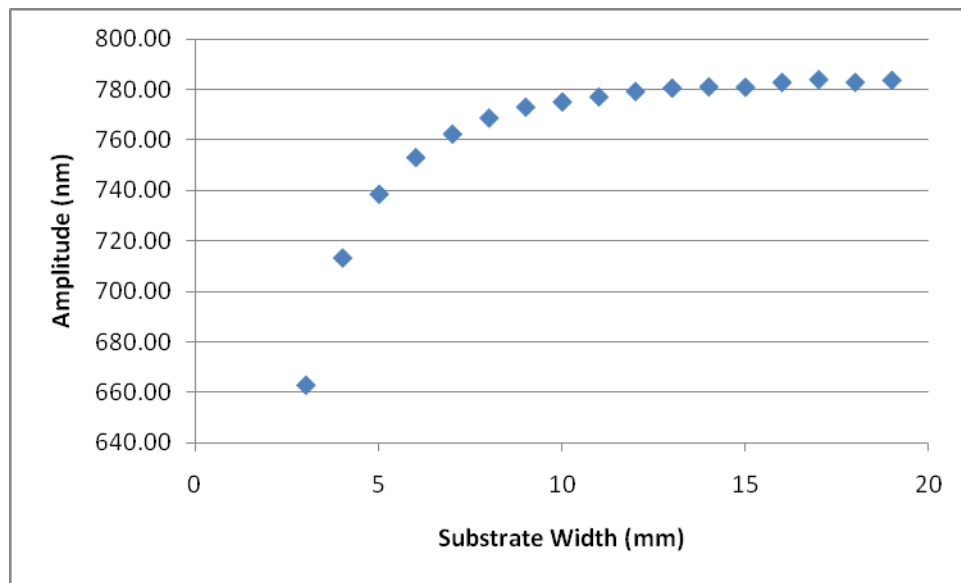


Figure 26. Amplitude as a function of substrate width, length  $7.5 \times 10^{-4}$  m.



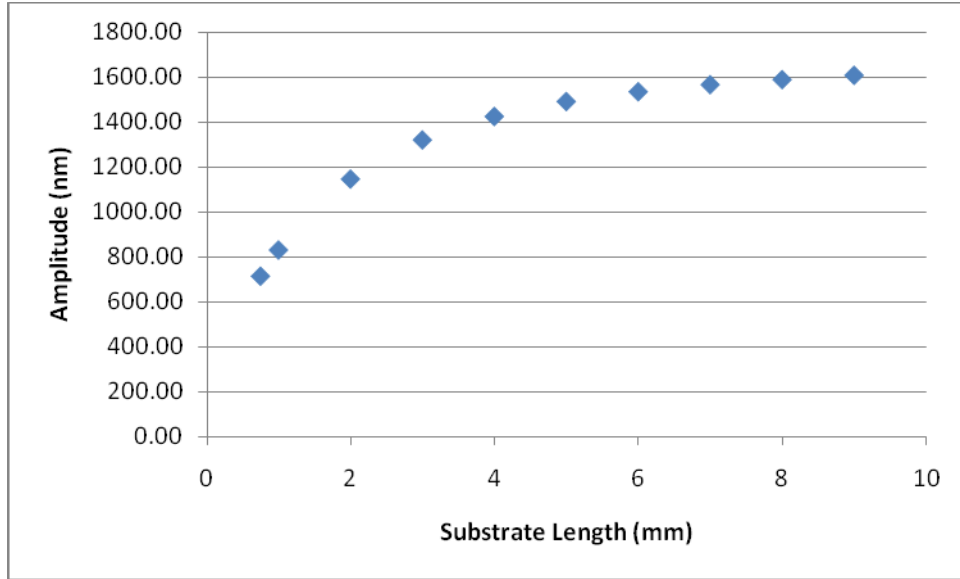


Figure 27. Amplitude as a function of substrate length, width  $4 \times 10^{-3}$  m.

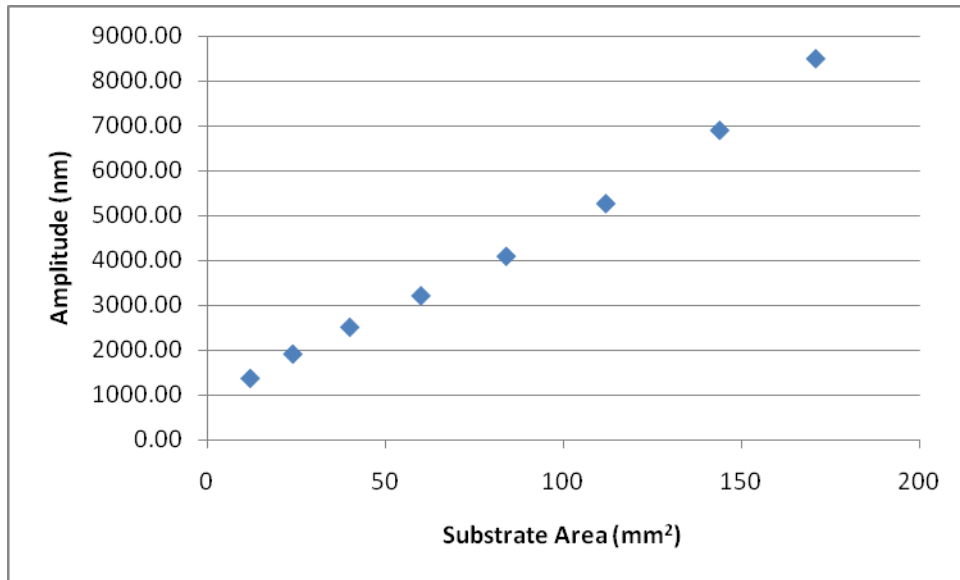


Figure 28. Amplitude as a function of substrate area.

The amplitude response shown above confirmed the hypothesis. Namely, the amplitude response increased as the substrate size increased. However, the maximum at 3.5 cm was not investigated due to time constraints. This maximum should be investigated further.

It is important to note that, with this model, the PML was not included, and the size of the cylindrical volume had been changed to accommodate the increase in the size of the substrate. I failed to examine how much acoustic energy would be reflected, given the increased size of the substrate. However, a few simulations with a PML inserted to ensure a free field effect were recalculated and the new simulations resulted in very minor changes to the amplitude.

THIS PAGE INTENTIONALLY LEFT BLANK

## **V. EXPERIMENTAL DATA**

### **A. ANECHOIC CHAMBER**

As mentioned earlier and displayed in Figure 20, LCDR Touse performed an experiment in an anechoic chamber with a similar sensor [20]. The experimental data and the simulated data for the bending frequency are in very close agreement. Both sets of data show a cosine dependence on the angle of incidence of the sound wave. However, further experimental data was not available as the sensor and readout were inadvertently damaged. Therefore, further measurements to confirm the simulations could not be performed.

### **B. RESONANT TUBE EXPERIMENT**

An experiment was conducted to demonstrate whether the sensor was a pressure sensor or a particle velocity sensor. A plastic tube was set up with a speaker at one end transmitting at the bending frequency of the sensor and the sensor connected to a rod at the far end as shown in Figure 29. A cork with a small hole was inserted in the end of the tube so that a standing wave could be created in the tube. The hole allowed the sensor and rod assembly to be moved in and out of the tube through pressure nodes and anti-nodes. Initially, a pressure microphone was inserted into the tube and the output was viewed on an oscilloscope. Locations of maximum and minimum pressure of the standing wave were marked on the exterior of the tube. Next, the suspected pressure gradient sensor was inserted so as to allow the sound wave to strike the sensor at normal incidence. The output was again examined on the oscilloscope.



Figure 29. Resonant tube experiment setup.

A pressure anti-node is an area of maximum pressure but with zero particle velocity. The particles move back and forth up to the pressure anti-node but do not cross it, thereby creating a pressure maximum. If the sensor were a pressure sensor then we would have seen a maximum response from it. But instead, we saw a minimal response. This indicated that the sensor was indeed a particle velocity sensor. We also moved the sensor to a pressure node that correlates to a minimum pressure or a maximum particle velocity. At this point we saw maximum response from the sensor. Therefore, we could conclude that the device that we have constructed is indeed a pressure gradient (particle velocity) sensor.

We then inserted the sensor into the tube so that the wave was hitting the sensor at an angle of 90 degrees. The sensor was moved through several pressure anti-nodes and pressure nodes. The response from the sensor was negligible again indicating that the sensor is a particle velocity sensor.

A third test was done whereby the sensor was placed at the opening of the tube and a travelling wave was allowed to strike the sensor. The sensor was placed at a set height and was rotated. The bending frequency and the rocking frequency were both examined. The oscilloscope output strongly resembled the output from the Multiphysics simulation for both bending and rocking frequencies. No actual measurements were taken as the sensor was damaged prior to taking any measurements. These measurements should be completed in the future to confirm the COMSOL model that was used in this thesis.

THIS PAGE INTENTIONALLY LEFT BLANK

## VI. CONCLUSIONS

As a follow-on to several previous theses at NPS on MEMS-based directional sensors, a non-acoustic model was developed and used for simulation of the sensor performance. The results of the non-acoustic model were consistent with findings of [11].

A new approach to the introduction of an acoustic wave into a Multiphysics simulation was developed. The selection of the Acoustic-Structure Interaction physics module and the introduction of the acoustic wave as a scalar variable resulted in an acceptable runtime for simulations. The free field effect was implemented by introducing a radiation condition on the outermost boundaries in all simulations. The simulated vibration amplitude as a function of incident angle of sound at the bending frequency showed good agreement with that of the experimental data provided by LCDR Touse [20]. It was also found that the inclusion of the substrate surrounding the sensor strongly affected the vibration amplitude. This indicates that proper packaging of the sensor is required for optimum performance. The use of a large substrate area may enhance the scattering effects requiring a larger fluid domain as well as inclusion of a PML to reduce the backscattering from the outer boundaries.

A sound pressure of one pascal was used for all simulations. However, Dristas 2008 found experimentally that the response is linear up to this pressure and thus, one can simply interpolate the amplitude to determine the amplitude response from a reduced incoming pressure.

Further work should be conducted on eliminating the 2D constraint on the sound source. This may require a larger acoustic domain volume and/or a more powerful desktop computer to perform the simulations. As well, future work should endeavor to more formally identify the amplitude of the rocking and bending modes to include the sum and difference of the plates.



THIS PAGE INTENTIONALLY LEFT BLANK

## LIST OF REFERENCES

- [1] R.N. Miles, D. Robert, and R.R. Hoy. “Mechanically coupled ears for directional hearing in the parasitoid fly *Ormia Ochracea*.” *The Journal of the Acoustical Society of America* vol. 98 pp. 3059–3070, December 1995.
- [2] COMSOL Multiphysics, (Version 3.5), (2008). [Computer Software]. [www.comsol.com](http://www.comsol.com). (December 2008).
- [3] Web site: “*Understanding Evolution*,” [http://evolution.berkeley.edu/evolibrary/news/061201\\_quietcrickets](http://evolution.berkeley.edu/evolibrary/news/061201_quietcrickets), (accessed 24 Nov, 2009).
- [4] W. Cade, “Acoustically orienting parasitoids: fly phonotaxis to cricket song,” *Science*, vol. 190, pp. 1313–1313, 1975.
- [5] Web site: “*Cornell Chronicle*,” <http://www.news.cornell.edu/chronicle/01/4.19.01/fly-hearing.html> (accessed 24 Nov, 2009).
- [6] A. Mörchen, J. Rheinlaender, and J. Schwartzkopff, “Latency shift in insect auditory fibers,” *Naturwissenschaften*, vol. 65, p. 657, 1978.
- [7] D. Robert, R.N. Miles, and R.R. Hoy. “Tympanal mechanics in the parasitoid fly *Ormia Ochracea*.” *Comp. Physiol A.*, vol.183 pp 443–452 183 (June 1998).
- [8] R.N. Miles, Q. Su, W. Cui, M. Shetye, F.L. Degertekin, B. Bicen, C. Garcia, S. Jones, and N. Hall. “A low-noise differential microphone inspired by the ears of the parasitoid fly *Ormia ochracea*.” *The Journal of the Acoustical Society of America* vol. 125 pp. 2013–2026, (April 2009).
- [9] G. Karunasiri, J. Sinibaldi, B. Kim, (2005). “NSF-MASINT Proposal Paper,” 2–14.
- [10] T.J. Shivok, “*Mems Polymumps\_Based Miniature Microphone for Directional Sound Sensing*.” Master’s thesis, Naval Postgraduate School, Monterey, CA, September 2007.
- [11] A. Dritsas, “*Characterization of the MEMS Directional Sound Sensor Fabricated Using the SOIMUMPS Process*.” Master’s thesis, Naval Postgraduate School, Monterey, CA, June 2008.
- [12] D. Chatzopoulos, “*Modeling the Performance of MEMS Based Directional Microphones*.” Master’s thesis, Naval Postgraduate School, Monterey, CA, December 2008.

- [13] N. Muamad, “*Characterization of MEMS a Directional Microphone with Solid and Perforated Wings.*” Master’s thesis, Naval Postgraduate School, Monterey, CA, June 2009.
- [14] K. Simsek, “*Developing a Capacitance Readout Circuitry for a Directional MEMS Sound Sensor and Sound Source Localization in a Sensor Network Environment.*” Master’s thesis, Naval Postgraduate School, Monterey, CA, June 2009.
- [15] Web site: “*Microphone,*” <http://en.wikipedia.org/wiki/Microphone> (accessed 24 Nov, 2009).
- [16] F. Fahy, *Foundations of Engineering Acoustics*. London: Elsevier Academic Press, 2007.
- [17] M. Rossi, *Acoustics and Electroacoustics*. London: Artech House, Inc. 1988.
- [18] L.E. Kinsler, A.R. Frey, A.B. Coppens, and J.V. Sanders. *Fundamentals of Acoustics*. New York: Wiley and Sons, 2000.
- [19] W. Zhang, and K. Turner. “Frequency dependent fluid damping of micro/nano flexural resonators: Experiment, model and analysis.” *Sensors and Actuators A: Physical.*, vol. 134pp. 594–599, July 2006:.
- [20] M. Touse, (Personal communications), January-December 2009.

## **INITIAL DISTRIBUTION LIST**

1. Defense Technical Information Center  
Ft. Belvoir, Virginia
2. Dudley Knox Library  
Naval Postgraduate School  
Monterey, California
3. Gamani Karunasiri  
Naval Postgraduate School  
Monterey, California
4. Steven Baker  
Naval Postgraduate School  
Monterey, California
5. Director General Maritime Equipment Program Management  
National Defence Headquarters  
Ottawa, ON  
CANADA
6. LCdr Stephen Harrison  
Naval Postgraduate School  
Monterey, California